

Summer Convective Precipitation Changes Over the Great Lakes Region Under a Warming Scenario



Key Points:

- The location of summer convective precipitation is shifted due to global warming
- Changes in lifting condensation level (LCL) and level of free convection (LFC) are the critical factors driving changes in convective precipitation
- The lowered LCL and LFC are controlled by the low-level moisture, not by air temperature

Correspondence to:










Z. Yang and Y. Qian,
zhao.yang@pnnl.gov;
yun.qian@pnnl.gov

Citation:

Yang, Z., Wang, J., Qian, Y., Chakraborty, TC, Xue, P., Pringle, W. J., et al. (2024). Summer convective precipitation changes over the Great Lakes region under a warming scenario. *Journal of Geophysical Research: Atmospheres*, 129, e2024JD041011. <https://doi.org/10.1029/2024JD041011>

Received 15 FEB 2024

Accepted 2 JUL 2024

Zhao Yang¹ , Jiali Wang² , Yun Qian¹ , TC Chakraborty¹, Pengfei Xue^{2,3} , William J. Pringle² , Chenfu Huang³, Miraj Bhakta Kayastha³ , Huilin Huang¹ , Jianfeng Li¹ , and Robert Hetland¹ 

¹Pacific Northwest National Laboratory, Richland, WA, USA, ²Environmental Science Division, Argonne National Laboratory, Lemont, IL, USA, ³Department of Civil, Environmental and Geospatial Engineering, Michigan Technological University, Houghton, MI, USA

Abstract To understand future summer precipitation changes over the Great Lakes Region (GLR), we performed an ensemble of regional climate simulations through the Pseudo-Global Warming (PGW) approach. We found that different types of convective precipitation respond differently to the PGW signal. Isolated deep convection (IDC), usually concentrated in the southern domain, shows an increase in precipitation to the north of the GLR. Mesoscale convective systems (MCSs), usually concentrated upwind of the GLR, shift to the downwind region with increased precipitation. Thermodynamic variables such as convective available potential energy (CAPE) and convective inhibition energy (CIN) are found to increase across almost the entire studied domain, creating a potential environment more favorable for stronger convection systems and less favorable for weaker ones. Meanwhile, changes in the lifting condensation level (LCL) and level of free convection (LFC) show a strong correlation with variations in convective precipitation, highlighting the significance of these thermodynamic factors in controlling precipitation over the domain. Our results indicate that the decrease in LCL and LFC in areas with increased convective precipitation is mainly due to increased atmospheric moisture. In response to the prescribed warming perturbation, MCSs occur more frequently downwind, while localized IDCs exhibit more intense rain rates, longer durations, and larger rainfall area.

Plain Language Summary To understand how summer rainfall might change in the Great Lakes Region in a warmer future climate, we performed several climate simulations using the Pseudo-Global Warming approach. We found that different types of heavy rain events react differently to the warming signal. Smaller convective rain events are projected to increase mainly over the northern domain, whereas the larger and sustained rain events are expected to increase over the eastern domain. The increase in rainfall is associated with low-level atmospheric moisture, which influences the atmospheric stability. With more moisture, the atmosphere becomes more unstable, leading to increased rainfall. The Great Lakes play an important role in providing moisture to their downwind regions, thereby affecting precipitation patterns.

1. Introduction

The Laurentian Great Lakes form the largest freshwater lake system in the world and significantly influence the local and regional hydroclimate (Bates et al., 1993; Bryan et al., 2015; Li et al., 2010; Notaro et al., 2013; Scott & Huff, 1996; Shi & Xue, 2019; Wang et al., 2022). These lakes contribute substantially to regional evaporation, which in turn facilitates precipitation over and around the lakes. According to Yang, Qian, et al. (2023), based on three different reanalyses, the local recycled moisture from the Great Lakes Region (GLR) account for about 35% of its precipitation. This precipitation plays a paramount role in regulating the water levels of the Great Lakes, thereby impacting socioeconomic activities and ecosystem services (Gronewold et al., 2013; Gronewold & Stow, 2014; Kayastha et al., 2022).

Several studies have examined precipitation climatology over the GLR, including the source of moisture for precipitation (Yang, Qian, et al., 2023), historical changes in precipitation characteristics (e.g., size and intensity), and projected changes in extreme precipitation under global warming (e.g., Basile et al., 2017; Byun et al., 2022; Cherkauer & Sinha, 2010; d'Orgeville et al., 2014; Mishra & Cherkauer, 2011; Michalak et al., 2013; Zobel et al., 2018, among others). These analyses have greatly enhanced the understanding of precipitation over the GLR and informed risk assessments for hydrometeorological extremes (e.g., drought and flooding) and their implications for the regional water-energy-food nexus in a warmer climate (Tidwell & Pebbles, 2015).

To obtain high-resolution future precipitation projection, the traditional method involves direct downscaling of global climate models (GCMs) using regional climate models (RCMs). However, this method is prone to biases inherited from the GCMs, which often have substantial discrepancies compared to historical observations. These biases are inevitably transferred to the high-resolution RCM simulations via lateral boundary conditions. An alternative approach is the pseudo-global warming (PGW) approach (Adachi & Tomita, 2020; Brogli et al., 2023; Gutmann et al., 2018; Hara et al., 2008; Hoogewind et al., 2017; Ito et al., 2016; Lynn et al., 2009; Rasmussen et al., 2011; Sato et al., 2007; Schär et al., 1996; Trapp et al., 2021; among others). This approach also falls under the concept of storyline approach by Shepherd (2019). It uses GCMs to provide information about mean changes in large-scale variables, which are then added as perturbation to a baseline historical climate (usually from reanalyses) to construct a future climate state. The resulting future climate state is then used to drive RCM to produce high-resolution future climate projections.

For the GLR, there remain significant uncertainties in accurately simulating precipitation patterns under warmer conditions. Both regional and GCMs struggle to realistically capture the hydrodynamics of the Great Lakes and their interactions with the atmosphere (Sharma et al., 2018; Xue et al., 2017, 2022). The representation of large lakes in climate models is challenging, limiting the predictive skill in simulating precipitation near the lakes. Global climate models (GCMs) often lack realistic representations partly due to their coarse resolution (Briley et al., 2021). Most state-of-the-art Coupled Model Intercomparison Project (CMIP) models (version 5 and 6) either do not represent the Great Lakes or have major inconsistencies in how the lakes are simulated in terms of spatial representation and treatment of lake processes (Briley et al., 2021; Minallah & Steiner, 2021; Notaro et al., 2022). Other limitations contributing to uncertainties include poor constraints on precipitation-related physical processes across climate models (Notaro et al., 2021), uncertainties in projected future climate scenarios for the region, and biases arising from the nonlinearities of hydrodynamic processes that are poorly described in numerical climate models.

Under future warming scenarios, higher air temperatures increase the saturation vapor pressure, usually leading to increased atmospheric water vapor. Therefore, future storms might become more intense and longer-lasting (Del Genio & Kovari, 2002; Kendon et al., 2012; O’Gorman & Schneider, 2009; Pall et al., 2007; Prein et al., 2017; Rasmussen et al., 2020; Sheffield & Wood, 2008; Trenberth et al., 2003). Future mean precipitation is expected to increase with warming (Pendergrass, 2020; Pendergrass et al., 2017; Pendergrass & Hartmann, 2014; Trenberth, 2011), with regional historical heavy precipitation reported to exceed the upper thermodynamic limit predicted by the Clausius-Clapeyron (CC) relation (Lenderink et al., 2017; Lenderink & van Meijgaard, 2008; Pendergrass, 2018; Prein et al., 2017; Westra et al., 2014). While mean precipitation is estimated to increase at a rate of $\sim 2\%–3\% \text{ K}^{-1}$ (Pendergrass, 2020; Pendergrass et al., 2017), extreme precipitation changes have been found to range between 7% and $10\% \text{ K}^{-1}$ of surface warming over the Great Lakes (d’Orgeville et al., 2014) and $11\%–14\%$ for western Europe (Lenderink and van Meijgaard, 2010).

To understand future changes in precipitation, studies have explored the underlying physical mechanism. Most studies used convective available potential energy (CAPE) and convective inhibition (CIN) to quantify atmospheric stability, finding that both CAPE and CIN increase in a warming climate, which could affect the precipitation frequency and intensity (Diffenbaugh et al., 2013; Gensini & Mote, 2015; Mahoney et al., 2013; Rasmussen et al., 2020). Over the United States, robust increases in CAPE and CIN have been reported by Diffenbaugh et al. (2013) and Seeley and Romps (2015). In particular, increased CIN acts as a balancing force, suppressing weak to moderate convection and allowing CAPE to build to extreme levels, potentially leading to more severe convection (Rasmussen et al., 2020). Rasmussen et al. (2020) also revealed that temperature plays an indispensable role in these thermodynamic environments. Similarly, Chen et al. (2020) demonstrated that low-CAPE and low-CIN conditions are projected to decrease in a warmer climate, resulting in fewer light to moderate precipitation events. Conversely, heavy precipitation events are projected to increase due to their increased probability under given CAPE and CIN conditions. To better understand how CAPE and CIN change in a warmer climate, Chen et al. (2019) found that the CAPE increase is mainly due to a moister low-level atmosphere, which leads to more latent heat and buoyancy, enabling easier lifting of parcels above the LFC. On the other hand, enhanced CIN over land results from reduced low-level relative humidity (RH), whereas over oceans, slightly increased RH weakens CIN (Chen et al., 2019). Such opposite response of CIN to future warming between land and water bodies makes it interesting to understand how climate change will affect precipitation over the GLR, a region comprising both land and water bodies.

While changes in overall precipitation and its extremes under future warming have been studied, little is known about how different precipitation types will change in the future. A recent study focusing on mesoscale convective systems (MCSs) over the Central United States revealed that the increase in future rainfall is primarily attributed to convective rainfall, with varying contributions from deep convective cores and wide convective cores, while broad stratiform regions show little increase (Dougherty et al., 2023). Historically, rainfall produced by MCSs and non-MCS, including the isolated deep convective cores (IDCs), has vastly different characteristics (Li et al., 2021). By definition, MCSs have larger spatial coverage and longer lifetimes compared to IDCs, although their rainfall rates are similar. Therefore, the hydrologic response of MCSs and non-MCSs could be very different (Hu et al., 2020). For example, MCS precipitation might result in more surface and subsurface runoff, while IDC precipitation may contribute more to evapotranspiration (ET). The difference in hydrologic response is mainly attributed to rain intensity (Hu et al., 2020). Over the GLR, different types of rainfall would lead to different partitioning into runoff or evaporation, potentially resulting in different water levels even with the same total precipitation amount. Moreover, MCSs are mostly upwind, while IDCs are downwind of the GLR based on historic observations (Wang et al., 2022). Hereafter, upwind refers to the south and southwest sides of the lakes, and downwind to the north and northeast, in line with the prevailing wind direction. In future warming and increased moisture conditions over the entire GLR, the spatial pattern of MCS and IDC may also change.

Despite previous studies on future precipitation changes over the GLR, several limitations remain: (a) Most dynamical downscaling studies use GCMs as boundary forcing, which may not properly represent lakes since lakes are not well resolved in GCMs, as discussed earlier; (b) coarse model resolution inevitably requires the use of convection parameterization, potentially hampering accurate precipitation representation; (c) previous studies using the PGW (Schär et al., 1996) approach usually adopt an ensemble mean of multiple Earth system models (ESMs), preventing uncertainty quantification; (d) besides CAPE/CIN, other thermodynamic variables such as lifting condensation level (LCL; m) and level of free convection (LFC; m) are seldom discussed in future climate conditions; (e) changes in precipitation associated with different convection types in the future are rarely addressed. Motivated by the previous studies on future precipitation changes, the main objective of this study is to understand the physical mechanisms leading to respective changes in MCSs and IDCs over the GLR by examining the thermodynamic environment described by CAPE, CIN, LCL and LFC. Using high-resolution convection-permitting simulations and the PGW approach, we study these changes by the end of this century. We conducted a 12-member ensemble run, enabling quantification of uncertainties in future summer precipitation with regional climate simulations. This study contributes to a greater physical understanding of the future changes in different convection types over the GLR in a warmer climate.

2. Materials and Methods

2.1. Reference Data Sets

Three precipitation reference data sets are chosen to better validate the model performance and understand the potential discrepancy across different data products. The reference data sets are based on various data sources, including in situ measurement and remote sensing such as radar and satellite detection. The selection of the reference data is also driven by their availability and accuracy over the Great Lakes. Details of these data sets are described as follows.

2.1.1. Parameter-Elevation Relationships on Independent Slopes Model (PRISM)

PRISM compiles climate data from various monitoring networks with rigorous quality control, and serves as the official U.S. Department of Agriculture spatial climate data set. PRISM precipitation is available at 4-km resolution at daily time scale, factoring in terrain elements like location, elevation, coastal proximity, topographic facet orientation, vertical atmospheric layer, topographic position, and orographic effectiveness (Daly et al., 2008). PRISM data is only available over continental United States and not available over the lakes.

2.1.2. Stage IV Precipitation

Stage IV precipitation, based on radar and gauge data, is a near-real-time product processed by the Next Generation Weather Radar precipitation system and the National Weather Service River Forecast Center (RFC) precipitation processing system (Fulton et al., 1998; Seo & Breidenbach, 2002). The precipitation data is mosaicked data from the 12 RFCs, compiled by the National Center for Environmental Prediction (NCEP),

providing gridded precipitation estimates at 4 km with 1-hourly and 6-hourly intervals (Nelson et al., 2016). Nelson et al. (2016) confirmed its good performance for medium to heavy precipitation. The Stage IV precipitation suffers discontinuity issues due to varied processing algorithms at different RFCs, especially in the western US. Stage IV precipitation is available over both land and the lakes.

2.1.3. TRMM

The Tropical Rainfall Measuring Mission (TRMM) is a joint mission between National Aeronautics and Space Administration (NASA) and the Japan Aerospace Exploration Agency (JAXA) designed to monitor and study tropical rainfall (Huffman et al., 2007). Utilizing the 3B42 algorithm, it generates rain gauge-adjusted multi-satellite precipitation rates and root-mean-square precipitation-error estimates. The TRMM 3B42 data set offers 3-hourly precipitation data with a spatial resolution of 0.25°, covering the region between 50°S and 50°N since March 2000.

2.2. Modeling Approach

2.2.1. Pseudo-Global Warming Approach

Two sets of simulations were performed. The first set, referred to as CTRL, represents the historical baseline simulation driven by the European Centre for Medium-Range Weather Forecasts atmospheric reanalysis of the global climate, version 5 (ERA-5, Hersbach et al., 2020; details in Section 2.2.2). The second set is the PGW simulation, driven by future forcing derived from imposing changes in the ESMs on the baseline forcing. The difference between the two sets of simulations reveals how the historical climate would unfold in a warmer climate.

To construct the future forcing, a simple form can be expressed as:

$$\text{Future forcing} = \text{ERA-5} + \Delta\text{CMIP6}_{\text{ssp585}} \quad (1)$$

where *Future forcing* represents the boundary conditions used to drive the RCM to simulate the future climate, and $\Delta\text{CMIP6}_{\text{ssp585}}$ is the mean change derived from the CMIP6 ESMs, expressed as:

$$\Delta\text{CMIP6}_{\text{ssp585}} = \text{VAR}_{2071-2100} - \text{VAR}_{1981-2010} \quad (2)$$

where $\text{VAR}_{2071-2100}$ represents the selected variables in the future time slice (2071–2100) of a climate projection, and $\text{VAR}_{1981-2010}$ represents variables in the historical time slice (1981–2010). $\Delta\text{CMIP6}_{\text{ssp585}}$ represents the variables being perturbed in our PGW approach, including variables such as two-dimensional near-surface air temperature, skin temperature, sea-level pressure, surface pressure, and three-dimensional air temperature, specific humidity, and geopotential height.

We construct the $\text{VAR}_{1981-2010}$ and $\text{VAR}_{2071-2100}$ under the SSP585 scenario based on data availability (Table 1). SSP585 stands for the shared socioeconomic pathway 5 (SSP5), with an additional radiative forcing of 8.5 W/m² by 2100. SSP5 assumes extensive global market integration, driving innovation and technological advancement, but relying heavily on intensified fossil fuel exploitation, particularly coal, alongside a globally energy-intensive lifestyle (Riahi et al., 2017). The use of SSP585 is intended to achieve a high signal-to-noise ratio, allowing for a relatively robust study of climate change impacts. This high-emission scenario provides a strong contrast between the baseline and future climates, enhancing the detectability of climate change signals.

To minimize the impact of interannual variability, monthly values of the selected variables are averaged over 30 years in both historical and future period. These monthly values are then temporally interpolated to 6-hourly intervals between consecutive months to ensure a smooth transition and reduce abrupt changes at the start of each new month. The changes of zonal and meridional winds in the ESMs are not considered in our PGW approach. Among the ESMs, all project increases in both air temperature and specific humidity under global warming. E3SM-1-1 projects the largest warming (9.9 K), followed by CanESM5, while FGOALS projects the smallest warming (4.8 K), followed by MPI. Lake surface temperature is an important lower boundary condition when running the RCM for a season-long simulation (Wang et al., 2022). While the lakes may not be realistically represented, their changes are the only available data source. However, EC-Earth3 shows a much stronger and

Table 1
Information of the Selected 11 CMIP6 Models

CMIP6 ^a model	Abbreviation	Model full name (reference)
ACCESS-CM2 ¹	ACCESS	The Australian Community Climate and Earth System Simulator coupled model, version 2 (Bi et al., 2020)
CESM2-WACCM	CESM	The Community Earth System Model version 2 coupled with the Whole Atmosphere Community Climate Model, Version 6 (Danabasoglu et al., 2020)
CMCC-CM2-SR5	CMCC	The Euro-Mediterranean Centre on Climate Change (CMCC) coupled climate model with standard configuration (Cherchi et al., 2019)
CanESM5	CanESM5	The Canadian Earth System Model, version 5 (Swart et al., 2019)
E3SM-1-1	E3SM	The U.S. Department of Energy (DOE) new Energy Exascale Earth System Model, version 1.1 (Golaz et al., 2019)
FGOALS-f3-L	FGOALS	The Chinese Academy of Sciences (CAS) Flexible Global Ocean-Atmosphere-Land System (He et al., 2019)
GFDL-CM4	GFDL	The Geophysical Fluid Dynamics Laboratory's atmosphere-ocean coupled climate model, version 4 (Held et al., 2019)
IPSL-CM6A-LR	IPSL	The Institut Pierre-Simon Laplace (IPSL) climate model, version 6A with low resolution (Boucher et al., 2020)
MIROC6	MIROC	The Model for Interdisciplinary Research on Climate, version 6 (Tatebe et al., 2019)
MPI-ESM1-2-LR	MPI	The Max Planck Institute for Meteorology Earth System Model, version 1.2 with low resolution (Mauritsen et al., 2019)
NorESM2-LM	Nor	The coupled Norwegian Earth System Model, version 2 with low-resolution atmosphere–land and medium-resolution ocean–sea ice (Seland et al., 2020)

^aWe only use the “r1i1p1f1” variant of each selected CMIP6 model.

unreasonable lake surface warming compared to the surrounding land, as observed and compared with fully coupled atmosphere and 3-D lake models (Xue et al., 2020). Therefore, EC-Earth3 is excluded from our experiment.

2.2.2. Regional Climate Model (RCM) Setup

Our RCM is the Weather and Research Forecasting (WRF) model version 4.2.2 with the Advanced Research WRF dynamic core (Skamarock et al., 2008). The model domain is centered at 45.5°N and 85.0°W, covering the GLR with 544 × 485 grid points in the west–east and south–north directions, with a grid spacing of 4 km (Figure 1). There are 50 stretched vertical levels topped at 50 hPa. The WRF model incorporates the Thompson microphysics (Thompson et al., 2004, 2008), the Rapid Radiative Transfer Model for GCMs (RRTMG) longwave and shortwave schemes (Iacono et al., 2008), and the Unified Noah land surface model (Chen and Dudhia (2001). We opted not to use the Noah with multi-parameterization (Noah-MP, Niu et al., 2011) due to its slightly inferior

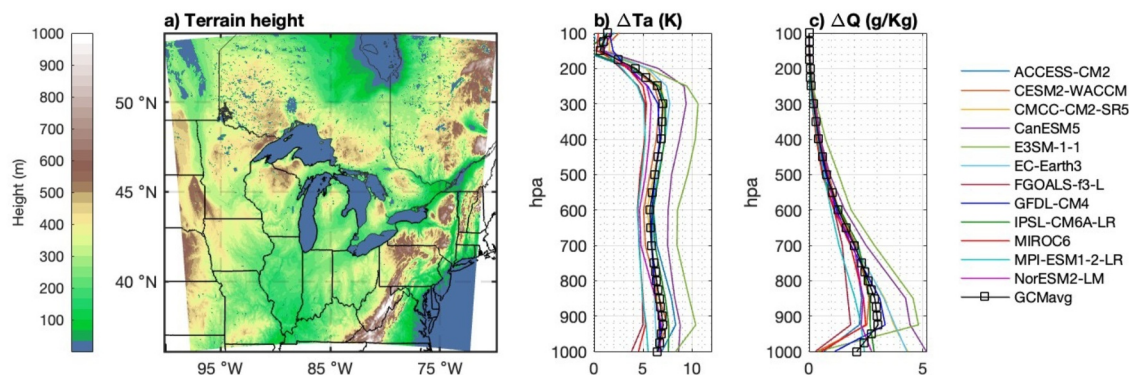


Figure 1. (a) WRF model domain with terrain height shown in shading. The domain spans 2172 km west-east and 1,936 km south-north. (b–c) Domain averaged seasonal mean difference in air temperature (Ta) and specific humidity (Q) between future (2071–2100) and historical (1981–2010) period in each of the selected ESMS.

performance compared to Noah for our simulation period. Conducting a comprehensive evaluation of all possible physics combinations in Noah-MP would involve over 1,700 model realizations (Arsenault et al., 2018; Niu et al., 2011), which is beyond the scope of our current study. However, it's important to note that recent advancements in Noah-MP's groundwater table dynamics have significantly improved the model's accuracy in simulating precipitation and temperature over the Midwest United States (Barlage et al., 2021; Liu et al., 2017). The Mellor–Yamada–Janjić (MYJ) (Janjić, 1990, 1994) planetary boundary layer (PBL) scheme and Monin–Obukhov surface layer scheme are also used, coupled with an updated multilayer building environment parameterization model and a multilayer building energy model (BEP_BEM, Salamanca et al., 2010, Salamanca & Martilli, 2010). While the use of urban models coupled to climate models requires higher computational costs, Wang et al. (2023) found that such coupled modeling can better captures urban locations' diurnal patterns of surface air temperature, skin temperature and RH. No sub-grid cloud cover or shallow cumulus parameterizations are used. No boundary nudging is applied, allowing the model to develop its own variability (e.g., spatial and internal variability) across the region.

For the baseline historical period, the initial and boundary conditions are constructed from 3-hourly 0.25° ERA-5. The lower boundary conditions for the lake, specifically, the lake surface temperature, are derived from the National Oceanic and Atmospheric Administration (NOAA) Great Lakes Surface Environmental Analysis (GLSEA) data set (Schwab et al., 1992) at a spatial resolution of 1.3 km. This setup was found by Wang et al. (2022) to produce better air temperature and heat flux compared with observations. The simulations started at 0000 UTC on 12 May 2018 and ended at 0000 UTC 1 September 2018 for both baseline and PGW scenarios. The resulting simulations were all analyzed starting 1 June 2018. 2018 was chosen because it was a neutral year for the GLR, and its MCS and IDC patterns matched the long-term average (Wang et al., 2022).

For the future scenarios, we conducted a total of 12 WRF PGW ensemble runs: 11 driven by the newly constructed initial and boundary conditions from each of the ESMS, and one driven by the ensemble mean of all chosen 11 ESMS. These 12 WRF ensemble runs allow us to study (a) the robustness of the future changes in different types of precipitation and the uncertainties caused by the various ESM forcing; (b) the difference between two sets of data sets: one is the WRF run driven by the ESM ensemble mean (hereafter PGW_GCMavg, a typical practice given limited computational resource available), and the other is the ensemble mean of all 11 individual WRF runs (PGW_RCMavg; this requires more computing resources but allows us for a more thorough examination of uncertainties).

2.3. Precipitation Decomposition

As introduced in Section 1, different convective systems show clearly different temporal and geospatial patterns over the GLR as well as the central and eastern continental United States (Li et al., 2021). While both MCS and IDC rainfall amount nearly doubled during the spring and summer (~100 mm) compared to the autumn and winter (~56 mm), MCS occurs earlier and over upwind of GLRs, and IDC occurs later and downwind of GLRs (Wang et al., 2022). Therefore, it is important to distinguish the different types of these storms over GLR. We applied the Flexible Object Tracker (FLEXTRKR) algorithm, developed by Feng et al. (2018, 2019) and enhanced by Li et al. (2021). Compared with other tracking algorithms (e.g., Prein et al., 2020; Workoff et al., 2012), which only examine the horizontal dimensions, FLEXTRKR identifies the three-dimensional structure of convective systems and can distinguish different convective systems such as the MCS and IDC. By tracking the MCS and IDC in the baseline simulation and future projections, we analyze how the MCS and IDC characteristics, including intensity, life length, initiation location, number of events, rainfall area and total rainfall amount would change under the PGW scenarios.

The criteria for identifying MCSs are (a) a cold cloud system (CCS) with contiguous areas of brightness temperature $T_b < 241$ K covering at least 6×10^4 km² and containing a precipitation feature (PF; contiguous regions of convective and stratiform echoes defined by the SL3D algorithm (Starzec et al., 2017) and precipitation rate > 1 mm hr⁻¹) with at least 100 km length in its major axis; (b) a convective feature with at least 45 dBZ radar reflectivity at any vertical level; (c) both (a) and (b) are satisfied for more than 6 hr. The criteria for IDCs are (a) a CCS with at least 64 km²; (b) at least 1 hr during the life cycle of the track when PF and convective core features (CCF, continuous updraft or convective areas with precipitation > 0 mm h⁻¹) are present (major axis lengths ≥ 4 km). In addition, for each IDC event, the CCS-based lifetime of associated merge and split tracks cannot surpass the lifetime of the IDC event.

2.4. Thermodynamic Environment

In this study, thermodynamic variables, including CAPE, CIN, LCL and LFC are derived from the WRF output. Here we use the most unstable CAPE (MUCAPE) which is a measure of instability in the troposphere that represents the total amount of potential energy available to air parcel with the maximum equivalent potential temperature within the atmosphere. The equivalent potential temperature represents the temperature that an air parcel would have if all its water vapor condensed, releasing the associated latent heat, and the parcel was then moved adiabatically to a pressure level of 1,000 hPa. To find the MUCAPE, air parcels from various pressure surfaces within the lowest 300 hPa in the atmosphere are released and the trajectory of a parcel that produces the maximum amount of CAPE has the most unstable CAPE. A parcel is defined as a 500-m deep parcel, with actual temperature and moisture averaged over that depth. For simplicity, we refer MUCAPE to CAPE hereafter unless otherwise noted. CIN is defined as the accumulated negative buoyant energy from the parcel starting point to the LFC. It is the amount of energy inhibiting convection and can help determine whether an environment is conducive or unfavorable for promoting convection development. In fact, as demonstrated in Rasmussen et al. (2020), CIN and CAPE are important indicators for convections. Environment with low CIN and high CAPE likely promotes convections but with limited strength. Environments with moderate CIN would allow CAPE to build up to higher levels; and with proper lifting mechanism, explosive convection can occur. However, if CIN is too large, then the inhibition or negative buoyancy is too strong for convection to break through, so convection is suppressed (Rasmussen et al., 2020). LCL is the level at which a parcel becomes saturated and is a good estimation of cloud base height. LFC is the level at which a lifted parcel begins a free acceleration upward to the equilibrium level due to positive buoyancy. Similar to CAPE and CIN, LCL and LFC are calculated based on the parcel with maximum equivalent potential temperature within the lowest 300 hPa of the atmosphere.

3. Results

3.1. Evaluation of Precipitation

Precipitation simulated by WRF for the baseline (summer of 2018) is first evaluated against the reference data sets to ensure the WRF model performance is reasonable for studying the future precipitation changes. Figures 2a–2d shows the comparison between TRMM, PRISM, Stage-IV, as well as WRF simulated total precipitation amount from June, July and August (JJA) of 2018. First of all, all 3 observational data sources show similar geospatial pattern of precipitation over land, with larger precipitation of about 7 mm day^{-1} over Iowa at the upwind of the lakes and even larger precipitation amount downwind of the lakes in Pennsylvania, Delaware. Although there is slight precipitation overestimation in Indiana and Ohio, the WRF model driven by ERA-5 can capture such overall dipole pattern in precipitation, including that over the Canadian side.

When divided into different convection types, the MCS precipitation is mainly located upwind to the west of the lakes (Figure 2e), whereas IDC precipitation is mainly distributed over the southeast of the domain in the reference data set (Figure 2f). Similarly, the non-convective precipitation is located over the southeast domain but with slightly larger magnitude (Figure 2g). The simulated precipitation associated with different convections can generally resemble that of the reference data set (Figures 2h–2j), although the MCS precipitation is slightly underestimated compared to the reference data sets (Figure 2h). Similar to the reference, the simulated IDC precipitation is also mainly located in the southeast of the domain but with slight overestimation over the south and southwest (Figure 2i). The non-convection is again well-captured by the baseline simulation (Figure 2j). It is worth noting that, while the FLEXTRKR algorithm can identify MCSs and IDC, it cannot distinguish tropical cyclones from non-convective precipitation (Li et al., 2021). Furthermore, FLEXTRKR may falsely classify convective precipitation as non-convective due to the brightness temperature threshold ($<241 \text{ K}$) used to define CCS and the relatively coarse temporal (hourly) resolution of the input data sets, causing the algorithm unable to capture IDC lasting less than 1 hr. This limitation explains the relatively large amount of non-convective precipitation observed over the domain. Overall, the baseline simulation is reasonable for further investigation of future precipitation changes using this modeling configuration.

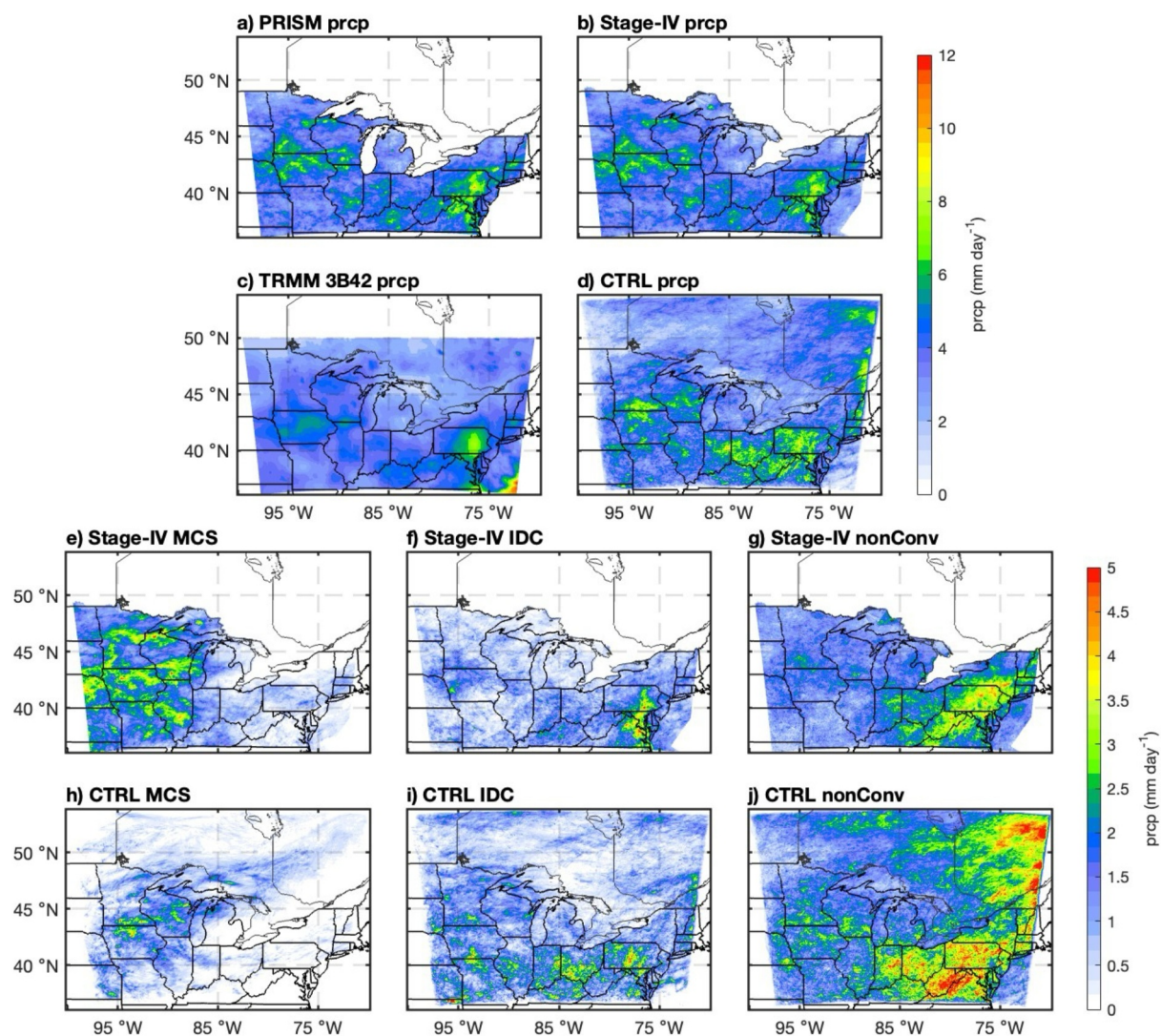


Figure 2. Evaluation of the simulated precipitation against reference precipitation data sets. JJA precipitation from panel (a) PRISM, (b) Stage-IV, (c) TRMM and (d) simulated precipitation from the baseline simulation (CTRL). (e–j) Evaluation of the different precipitation types against reference precipitation data sets. (e–g) are observation-based, and (h–j) are baseline simulated precipitation amounts for different types, namely MCS, IDC and non-convective precipitation.

3.2. Future Precipitation Changes

3.2.1. Overall Precipitation Changes

Precipitation in future scenarios and their changes compared with baseline are shown in Figure 3. Overall, the future summer precipitation shows clearly different spatial patterns with decreased precipitation upwind of the Great Lakes Basin and increase over the northeast and southeast of the domain (Figures 3a and 3b and 3days-e). Downscaled simulations with forcing derived from individual GCM generally agree with the overall pattern, though with slightly different magnitudes. For example, simulation driven by CanESM5, CMCC and FGOALS show the least, moderate and largest amount of precipitation increase (Figures 3g–3i). It is also noteworthy that the spatial distribution of summer mean precipitation is very similar between PGW_GCMavg and PGW_RCMavg, although PGW_RCMavg shows a smoother spatial pattern because it averages across the 11 WRF simulations driven by individual ESMS. In fact, when we look at individual rainstorm events, PGW_GCMavg can still capture some rainfall peaks that are forced by individual ESM forcing. This indicates that, with limited computing resources, it can be reasonable to conduct the WRF simulations with the ESM ensemble mean. However, to quantify the uncertainty due to different forcings, it is still needed to run WRF simulations driven by individual ESMS, as we do in this study. For instance, the standard deviation of

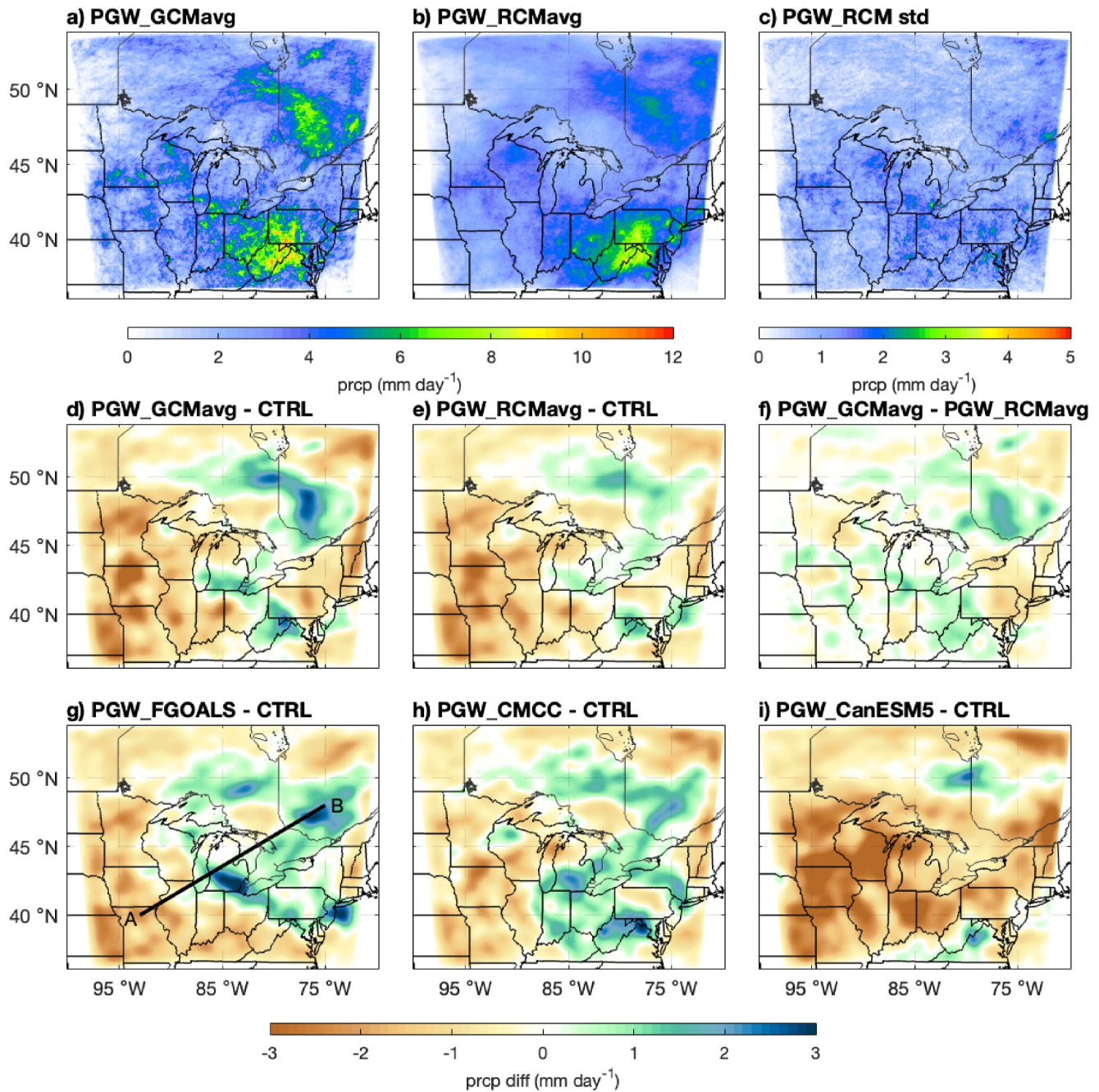


Figure 3. Simulated precipitation in future warmer climate and its changes against the baseline simulation. (a–b) Simulated precipitation from PGW_GCMavg and PGW_RCMavg, (c) standard deviation from the ensemble of 11 ESMs, (d–e) precipitation difference between PGW_GCMavg, PGW_RCMavg and baseline, (f) the difference between PGW_GCMavg and PGW_RCMavg (PGW_GCMavg minus PGW_RCMavg), (g–i) difference between the selected coolest (FGOALS), moderate (CMCC), and warmest (CanESM5) ESM and the baseline simulation. The black line represents the cross-section shown in Figure 5.

precipitation suggests that there might be larger uncertainties in the simulated precipitation over northeast Wisconsin, south Michigan (Figure 3c). Nevertheless, the summer averaged precipitation changes produced by PGW_GCMavg and PGW_RCMavg are very similar in spatial patterns, with spatial correlation of 0.87 (Figures 2e and 2f).

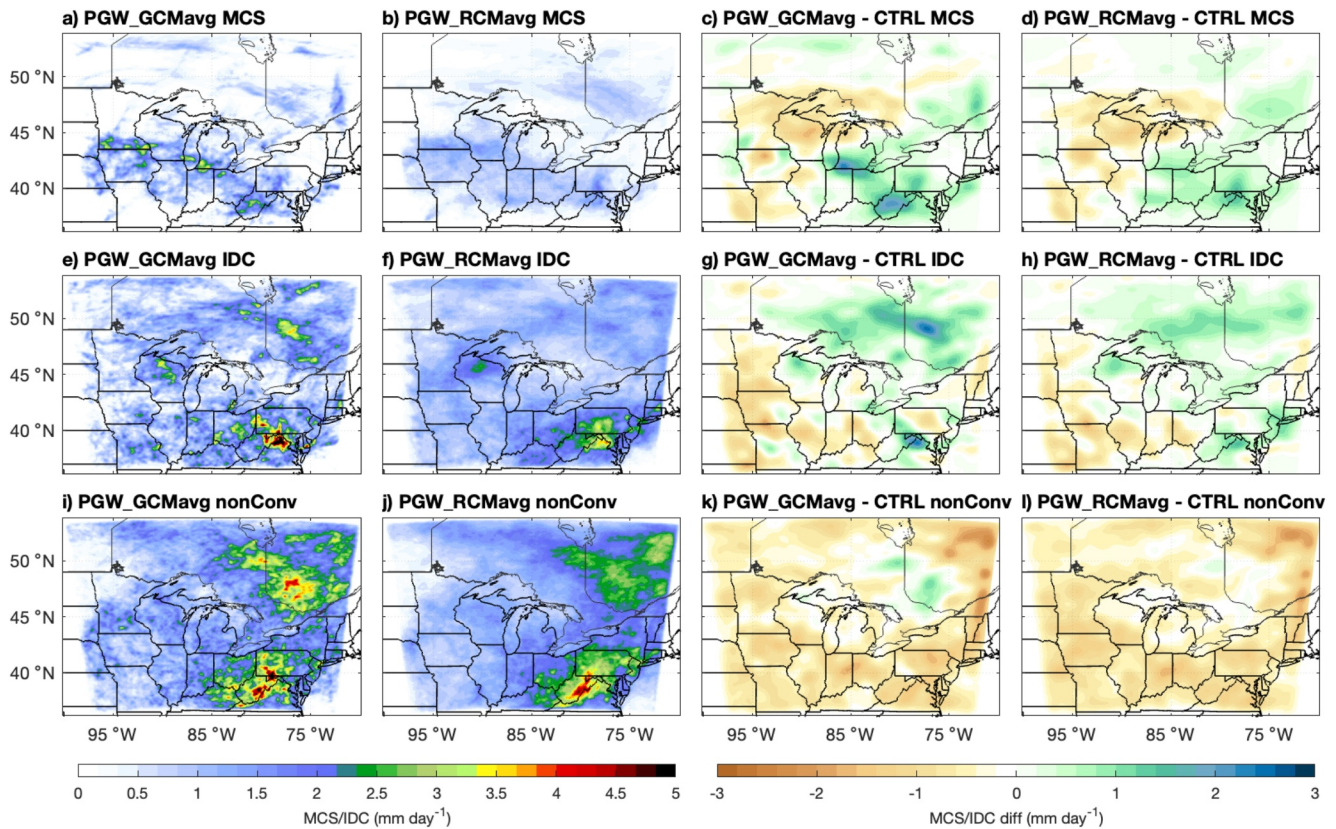


Figure 4. Spatial distribution of the different precipitation types and their changes from the baseline simulation. (a–b) Simulated MCS precipitation in panel (a) PGW_GCMavg and (b) PGW_RCMavg. (c–d) Difference in MCS precipitation between (c) PGW_GCMavg and CTRL (d) PGW_RCMavg and CTRL. (e–h) Similar as (a–d) but for IDC precipitation. (i–l) Similar as panels (a–d) but for non-convective precipitation.

3.2.2. Changes in MCSs and IDCs and Their Characteristics

This section examines the future changes associated with different convection types, that is, the MCSs and IDCs. Figure 4 displays the distribution of MCS precipitation in warmer climate (Figures 4a and 4b) and the changes in future projected by PGW_GCMavg and PGW_RCMavg (Figures 4c and 4d). In the historical period, MCS precipitation is distributed mainly over the west portion of the domain, and slightly extends to the northeast of the GLR (Figure 2h). In warmer climate, precipitation associated with MCSs seems to shift to the east with increase mainly over the southeast and east side of the domain, resulting in a decrease over its original location (Figures 4a–4d) and an increase over downwind of GLR. Such spatial shift is clear and consistent in all WRF ensemble runs (not shown).

Figures 4e–4f displays the distribution of IDC precipitation and the changes projected by PGW_GCMavg and PGW_RCMavg (Figures 4g and 4h). Historical IDC precipitation spreads over the entire domain, with larger portion to the south and southeast side of the domain (Figure 2i). In the future scenarios, the IDC precipitation shifts further to the north and northeast side of the domain (Figures 4g and 4h) and agrees among all individual ensemble model (not shown). The non-convective precipitation generally shows a decreasing pattern almost over the entire domain, with the exception of the northeast domain (Figures 4i–4l). Notably, although variabilities exist in the spatial distribution of different convective precipitation among different ensemble members, the general pattern agrees reasonably well between PGW_GCMavg and PGW_RCMavg, again supporting the applicability of using ensemble mean of ESM deltas as forcing to downscale future scenarios.

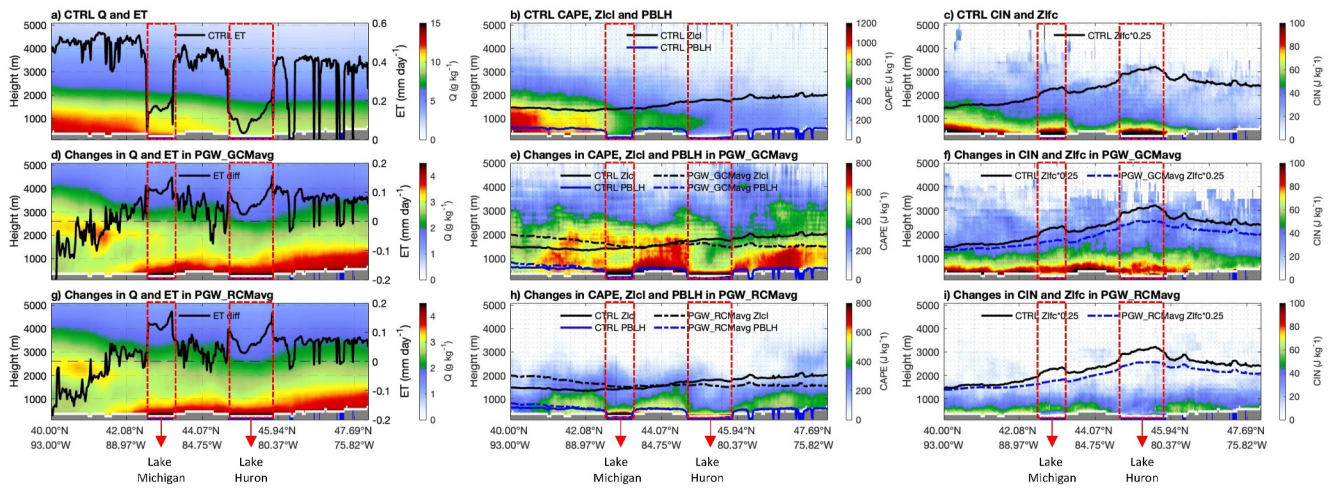


Figure 5. Cross-sectional analysis along the cross-section shown in Figure 3g, which pass over southern Lake Michigan (shown between 42.08 and 44.07 N, smaller red dash box on the left) and Lake Huron (shown between 44.07 and 46 N, larger red dash box on the right). (a) Color shading indicates the specific humidity (Q , units: g kg^{-1}), the black curve indicates the evapotranspiration (ET) along the cross-section from the land and water bodies (magnitude corresponds to y-axis on the right). (d) and (g) color shading shows the difference in specific humidity, while the black curve indicates the difference in ET between PGW_GCMavg, PGW_RCMavg and baseline simulation, respectively. (b, e, and h) are similar to (a, d and g) expect that the color shading displays the CAPE, the black curve shows the height of LCL (magnitude corresponds to the left y-axis), the blue curves show the planetary boundary height. (c, f, and i) are similar to panels (b, e, h) except that the color shading shows the CIN and black curve shows the level of LFC multiplied by a factor of 0.25. LFC usually has a much larger magnitude than LCL, therefore, LFC is multiplied by a factor to make them shown in the same height range.

3.2.3. Physical Mechanisms

3.2.3.1. Identifying Key Thermodynamic Variables

This section aims to understand the mechanisms for the MCS and IDC precipitation changes at the specific locations as identified in the previous section. To do so, we first study the environmental conditions for overall precipitation by examining the thermodynamic variables including CAPE, CIN, LCL and LFC. This is done for the entire domain as well as after separating it into upwind and downwind regions to specifically understand the moisture contribution of the Great Lakes. We then study these thermodynamic factors separately for MCS and IDC events, and also investigate the characteristic changes in MCS and IDC to understand the common and unique factors causing their respective future changes.

To explore the mechanisms of the overall precipitation changes, Figure 5 shows the cross-section analysis of thermodynamic environment from the upwind to the downwind of the Great Lakes. The CAPE and CIN shown here represents the amount of available potential energy or inhibition from each level to the equilibrium level, and is different from MUCAPE and MUCIN, which represent the maximum out of these levels. In the baseline simulation, the upwind region is featured with high CAPE, relatively low LCL and LFC compared to the downwind region (Figures 5a–5c), and therefore more conducive for convection at the upwind regions (Figure 2d). In a warmer climate, the existence of the Great Lakes increases evaporation and acts as a moisture source for the surrounding and downwind regions (Figures 5d–5f and 5g–5i). As a result of the moisture increase, it causes an increase in CAPE especially at the immediate downwind of water bodies (Figures 5e and 5h). Meanwhile, LCL also shows a decrease, whereas PBL height (PBLH) remains the same (Figures 5e and 5h) downwind of GLR, suggesting an increased likelihood of cloud formation. Moreover, LFC shows an even larger decrease in this downwind region (Figures 5f and 5i). Overall, the warming-induced changes in thermodynamic environment leads to a more stable environment at the upwind with higher LCL and larger CIN; and more unstable at the downwind regions with lower LCL and LFC as well as larger CAPE and ET. These changes ultimately decrease precipitation at the interior inland region at the upwind and increase precipitation at the downwind of the Great Lakes. These changes may explain why MCS decreases upwind and IDC increases downwind of the GLR. We also examined changes in wind to assess how alterations in wind influence evaporative change. Our findings suggest that these wind changes near the surface are almost negligible, suggesting that changes in ET are mainly caused by the gradient between the surface and the lower atmosphere (not shown).

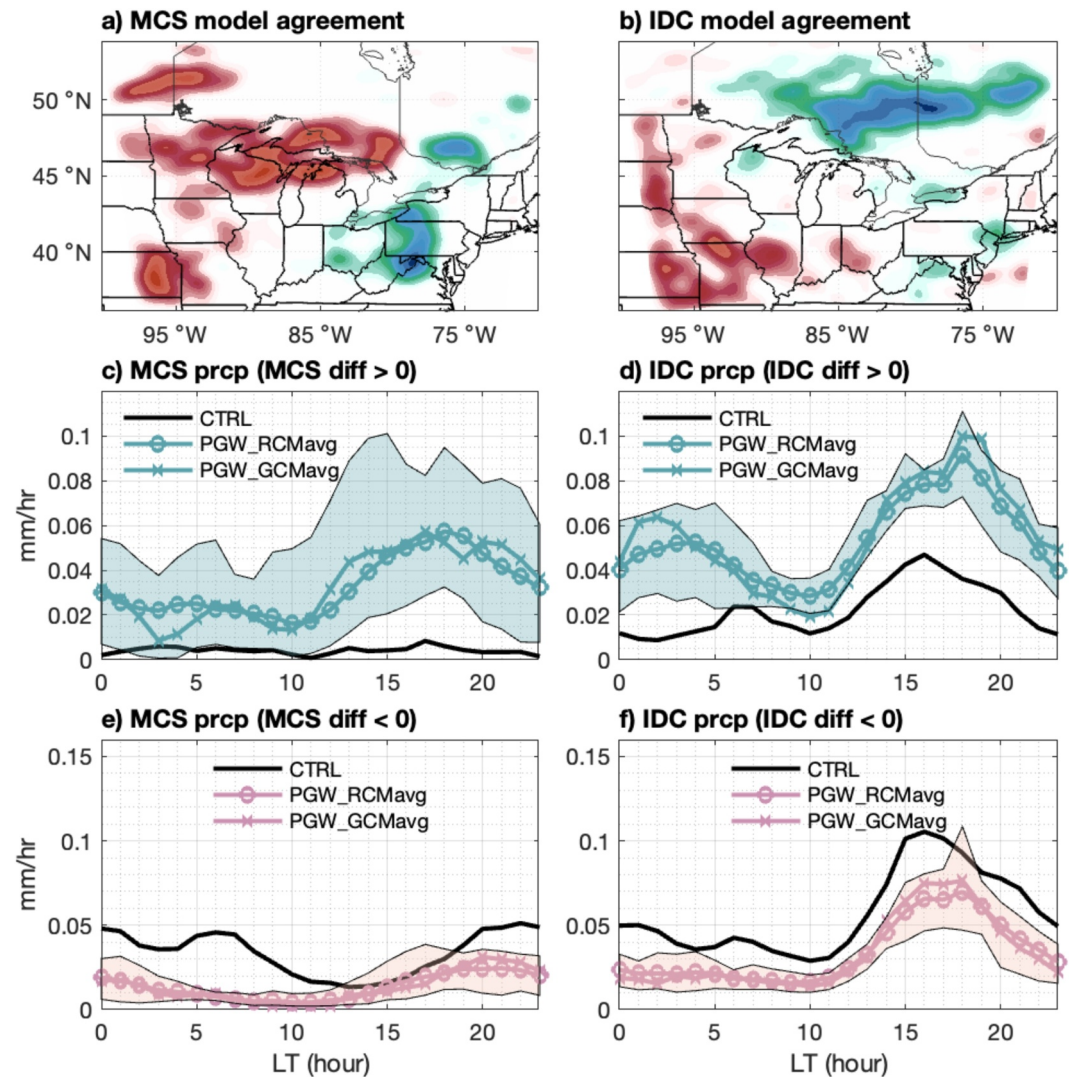


Figure 6. Identification of location and time where MCS and IDC precipitation increase and decrease due to PGW perturbation. (a) Model agreement of MCS precipitation change due to the PGW perturbation, red and blue indicates MCS precipitation decrease and increase consistently among all ESM ensemble members. (c) Diurnal cycle of MCS precipitation over places where all models agree that MCS is increased in the PGW simulations (i.e., blue region in panel (a)). Black curve represents the CTRL simulation, the blue shading indicates the ensemble range, blue line with circle represents the mean of individual models (i.e., PGW_RCMavg), blue line with cross represents the simulation forced by the ESM mean as forcing (i.e., PGW_GCMavg). (e) Same as (c) except the diurnal cycle of MCS precipitation is over places where MCS is decreased (i.e., red region in panel (a)). (b, d, and f) are similar as panels (a, c, and e) but for IDC.

Figures 6a and 6b display regions with the same sign of changes as a result of warming for MCS and IDC precipitation among all individual ensembles. Moreover, the diurnal cycles of MCS and IDC precipitation over the identified regions are shown to pinpoint the time at which the largest differences in MCS and IDC occur. Figures 6c and 6d show that over places where MCS or IDC precipitation is increased, the largest differences occur both around local early evenings around 18 local time (LT, corresponds to 00 UTC). Alternatively, when MCS or IDC precipitation is decreased in the PGW simulations, as shown in Figures 6e and 6f, MCS precipitation decreases the most near local midnight to early morning, while IDC precipitation decreases the most near the same time. Nevertheless, we select thermodynamic environment at 18 LT to further understand the corresponding changes, both increase and decrease, in MCS and IDC precipitation. We have also looked at other timings and the general conclusions remain the same regardless of the timing selected.

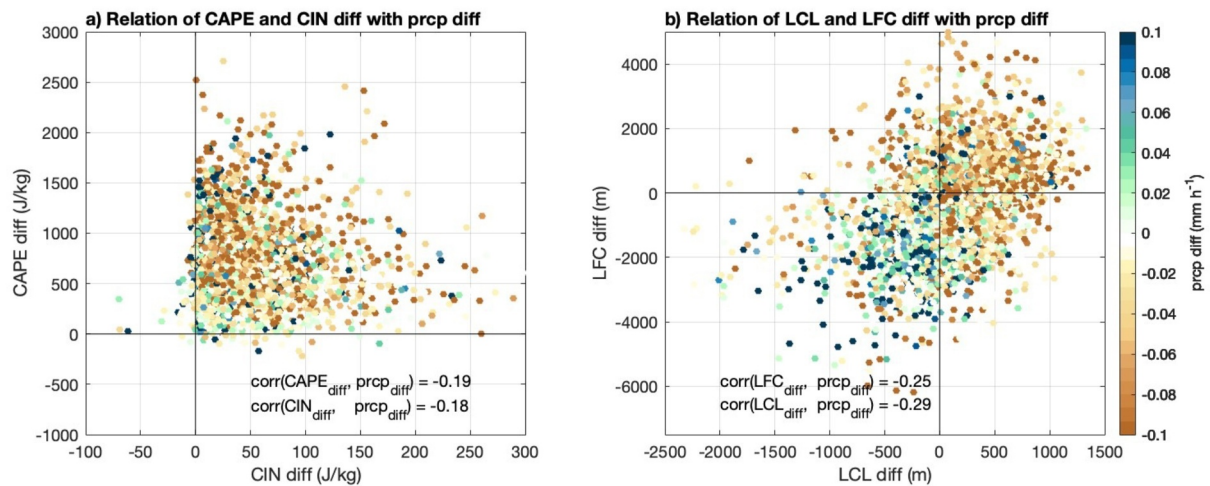


Figure 7. The relationship between changes in CAPE and CIN and changes in precipitation (left), and between changes in LCL and LFC and changes in precipitation (right). Color represents precipitation increase (blue) or decrease (brown) due to the PGW perturbation. Considering both increase and decrease in MCS and IDC, the data points are collected by averaging over the green or red regions in Figures 6a and 6b at 18 LT, respectively. For each day during the JJA season, there are 4 data points. For example, one data point is produced by averaging the difference in CAPE and CIN between PGW and CTRL simulation for red region in Figure 5a, which determines the x–y location, and color shaded by precipitation difference. Similarly. Another 3 data points are produced by averaging over the green region in Figure 6a and blue and red regions in Figure 6b, accounting for both increase and decrease in MCS and IDC for the same day. Same procedure will be repeated for the entire JJA season and for all PGW simulations to obtain the overall relationship between the changes in thermodynamic environment and precipitation. Numbers in the plot indicate the Spearman's rank correlation coefficient.

To further understand the role of each of these thermodynamic factors in modulating the future precipitation changes in both MCS and IDC, Figure 7 displays the relationships between changes in CAPE and CIN as well as LCL and LFC and changes in precipitation. Surprisingly, we found that, regardless of the precipitation types (MCS or IDC) and changes (increase or decrease), CAPE and CIN always increase, suggesting that CAPE and CIN may not be the factors determining precipitation changes. In other words, regardless of precipitation increase or decrease, the negative buoyant energy air parcels need to overcome before freely ascending is universally increased. Once air parcels become positively buoyant, air parcels are more unstable with more convective potential (i.e., CAPE). The greater values of CAPE and CIN in a warmer climate have also been reported in previous studies (Rasmussen et al., 2020). Interestingly, LFC and LCL demonstrate a relatively clearer relationship between their changes and precipitation changes. Specifically, when the LCL and LFC decrease (increase), there are precipitation increase (decrease), shown in Figure 7b. This is physically intuitive because with lower LCL and LFC it is easier for air parcels to form clouds and grow into organized convection.

In summary, we find that there is a precipitation decrease upwind of GLR, and a precipitation increase downwind. Such changes are promoted by an environment with increased ET, CAPE, and CIN, and lower LCL and LFC over and downwind of the Great Lakes (Figure 5). However, CAPE and CIN increase is not the determining factors of the precipitation increase, instead, lower LCL and LFC play the key role in increasing precipitation downwind of Great Lakes. We next examine how the warmer and moister (in terms of specific humidity) atmospheric, respectively and collectively, contribute to these changes seen in LFC and LCL.

3.2.3.2. Isolating the Effect of Temperature and Moisture on Thermodynamic Variables

LCL and LFC are derived as a function of vertical profiles of water vapor mixing, temperature, geopotential height, and surface pressure. When these input values from baseline or PGW simulations are plugged into the equation, the respective LCL and LFC can be obtained. In this study, to estimate the first order effects of temperature (moisture) on LCL or LFC changes, we swap the temperature (moisture) values from the baseline simulation with temperature (moisture) from the PGW simulations. These sensitivity calculations are designed such that no oversaturation would occur in either scenario while eliminating the need to re-run PGW simulations considering only temperature or moisture change.

Figure 8 shows the opposite effect of PGW-induced temperature and moisture on LCL and LFC changes for MCS precipitation (same for IDC; not shown). Based on Figure 7, we know that over places where precipitation is

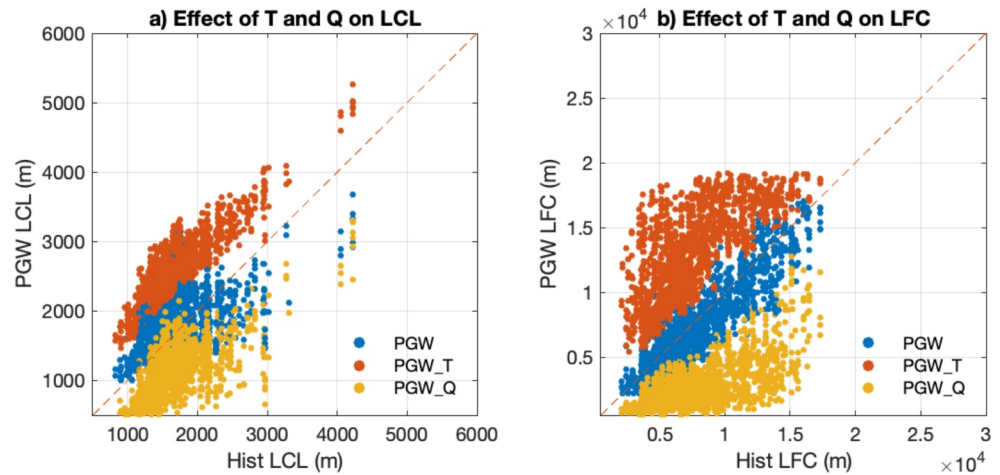


Figure 8. Scatter plots of LCL (left) and LFC (right) for baseline and perturbed calculations by changing air temperature only (indicated by orange color), and moisture only (yellow), respectively. The procedure of extracting data points is same as that in Figure 7.

increased (decreased) both the future LCL and LFC are decreasing (increasing). However, when we only change the air temperature based on our PGW simulation output, and keep everything else the same, it leads to a higher LCL and LFC, making it more difficult for convection to occur (i.e., PGW_T; red dots). On the contrary, the future moisture changes lead to a lower LCL and LFC, which can result in more conducive environment for convection to occur (i.e., PGW_Q; yellow dots). This is because with warmer temperature, there are much higher saturated water vapor pressure following the CC relation. If specific humidity is fixed, then RH will be decreased, making the vapor pressure deficit larger and more difficult to reach saturation in the lower atmosphere, resulting in higher LCL and LFC. Conversely, higher moisture amount with fixed temperature gives rise to much higher RH and therefore lower LCL and LFC, and ultimately leading to more convective conducive environment.

This finding highlights the importance of low-level moisture for the formation of MCS precipitation, which has been also highlighted by previous studies (e.g., Peters et al., 2017; Schumacher & Peters, 2017; Yang, Varble, et al., 2023). Schumacher and Peters (2017) found that the low-level moisture strongly regulates the amount of precipitation produced by MCSs, that is, a 3.4% increase in vertically integrated water vapor leads to an increased by nearly 60% in the area integrated MCS precipitation. Given the importance of low-level moisture in conditioning the thermodynamic environment (Schumacher & Peters, 2017; Yang, Varble, et al., 2023), vertical profiles of RH are shown in Figure 9. For places where MCS or IDC are increased (1st and 3rd column), the RH profiles of PGW simulations are very similar to or slightly smaller than that of the baseline simulations. This is because the temperature is much warmer in PGW simulations, and the amount of moisture carried by the atmosphere is much more in the PGW simulations than the CTRL simulation. If a proper lifting mechanism exists along with the much higher CAPE (Figures 5e and 5h), both MCS and IDC precipitation would be increased in PGW simulations compared to the baseline. On the other hand, for places where MCS or IDC are decreased (2nd and 4th column), the RH profiles in PGW simulations are much drier than the baseline simulations. Such drier conditions lead to higher LFC/LCL (Figures 5 and 7), making it difficult for convection to occur, which ultimately cause less precipitation associated with MCS and IDC events (Figures 4 and 6).

The analysis above suggests that the key thermodynamic factors that cause the precipitation increase overall is the lower LCL and LFC; and that the increased moisture in future is the main driver of such decrease in LCL and LFC. This mechanism is true for both MCS and IDC when study the entire domain as a whole. However, from Figures 3 and 4, we know that the changes in MCS and IDC are spatially distinct. Here we further examine the differences between these two types of precipitation changes. To explain the differences in spatial coverage of MCS precipitation between the baseline and the PGW simulations, Figure 10 displays all the MCS tracks from initiation to dissipation for the entire season. The MCS tracks agree with the overall spatial pattern of MCS precipitation amount (Figures 2h and 4a–4b). For example, MCS tracks gather towards the western portion of the domain with only two MCS events initiated in the south and southeast of GLR in the baseline simulation (Figure 10a). In contrast, in the PGW simulations, there are more tracks that originate over the central and

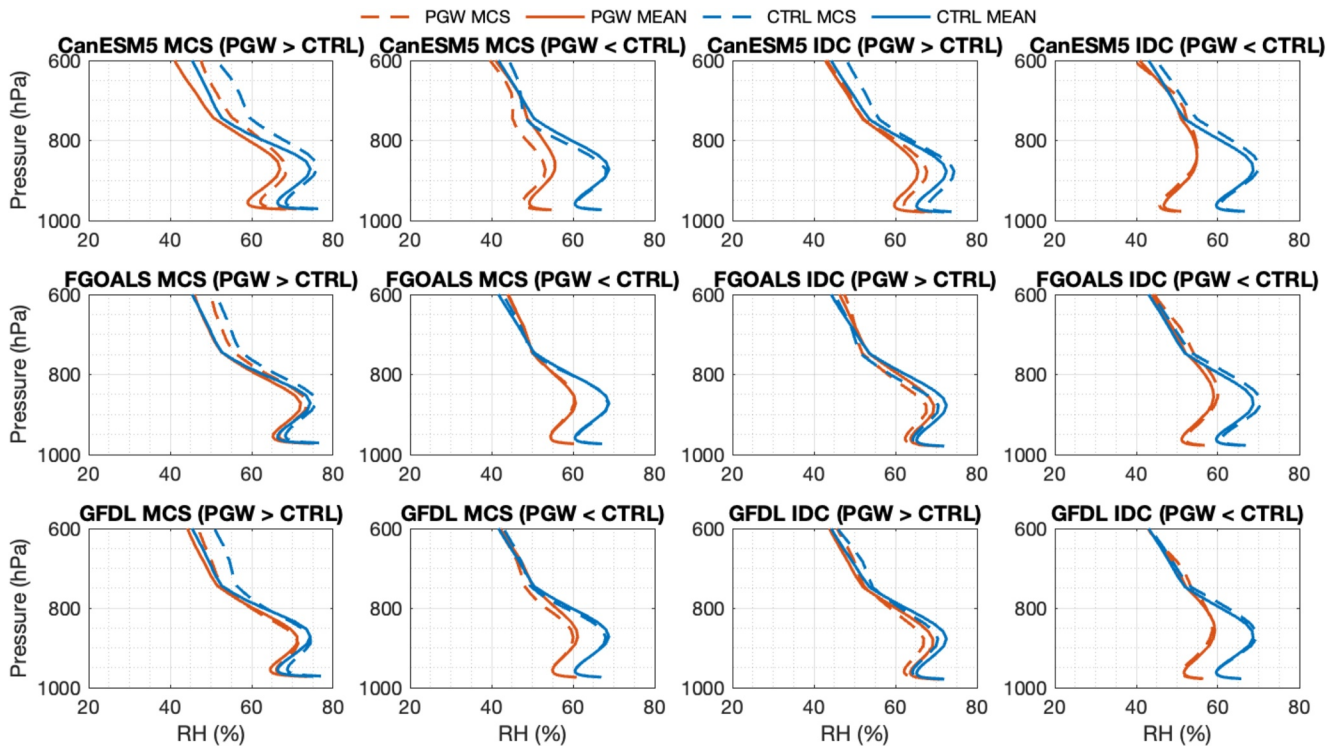


Figure 9. Relative humidity profiles over regions where MCS/IDC are increased (1st and 3rd columns) and decreased (2nd and 4th columns) for selected GCMs at 18 LT. All other GCMs show the same behavior and are not shown.

southern domain and bring precipitation to the southeast of GLR (Figure 10b), which explains the increase in MCS precipitation in Ohio, Pennsylvania and West Virginia (Figures 4c and 4d). MCS events are less frequent near the US-Canada border in Wisconsin and Michigan (Figures 10a and 10b), resulting in MCS precipitation decrease over these regions in PGW_GCMavg (Figures 4c and 4d). Over the entire domain, slightly fewer MCS tracks are observed in the PGW simulations relative to the baseline simulation.

Given their relatively short life length and travel distance, IDC initiation locations are considered to be good proxies for the IDC event locations. The total number of IDCs witnesses a 40% decrease from 8,887 in the baseline to 5,418 in PGW_GCMavg. The reduction in IDC frequency is consistent with increases in CIN, as the increased CIN acts to suppress weak to moderate convection (Rasmussen et al., 2020). We also found that the reduction is almost universal in the entire domain (Figures 10c and 10d). Nevertheless, there are still increase in IDC precipitation amount in PGW simulations over the domain as shown in Figures 4g and 4h. This increase is due to more intense precipitation rate, longer duration, and large spatial coverage (Figures 10e–10h). Therefore, the mechanisms for the changes in MCS and IDC precipitation in future are different. The shift of the MCS precipitation from upwind to downwind is mainly due to the changes in MCS tracks, whereas the increase of IDC precipitation can be explained by a combination of increase in precipitation intensity, duration and spatial coverage, despite the decreased frequency over entire domain.

4. Summary and Discussions

We performed an ensemble of regional climate simulations through the PGW approach to understand the future summer precipitation change over the GLR. Results show that the location of future precipitation is shifted for different convection types in the PGW simulations. More intense, long-lasting MCS induced precipitation move to the east and southeast of the GLR. Due to the shift in precipitation systems, there is a net precipitation decrease upwind and precipitation increase downwind of the Great Lakes. The variation in different convective precipitation is mainly associated with thermodynamic changes in LCL and LFC, rather than CAPE and CIN, although they are found to be increased almost over the entire domain, similar to those found in previous studies. This suggests that CAPE and CIN are not the determining factor in controlling the changes in precipitation. Instead,

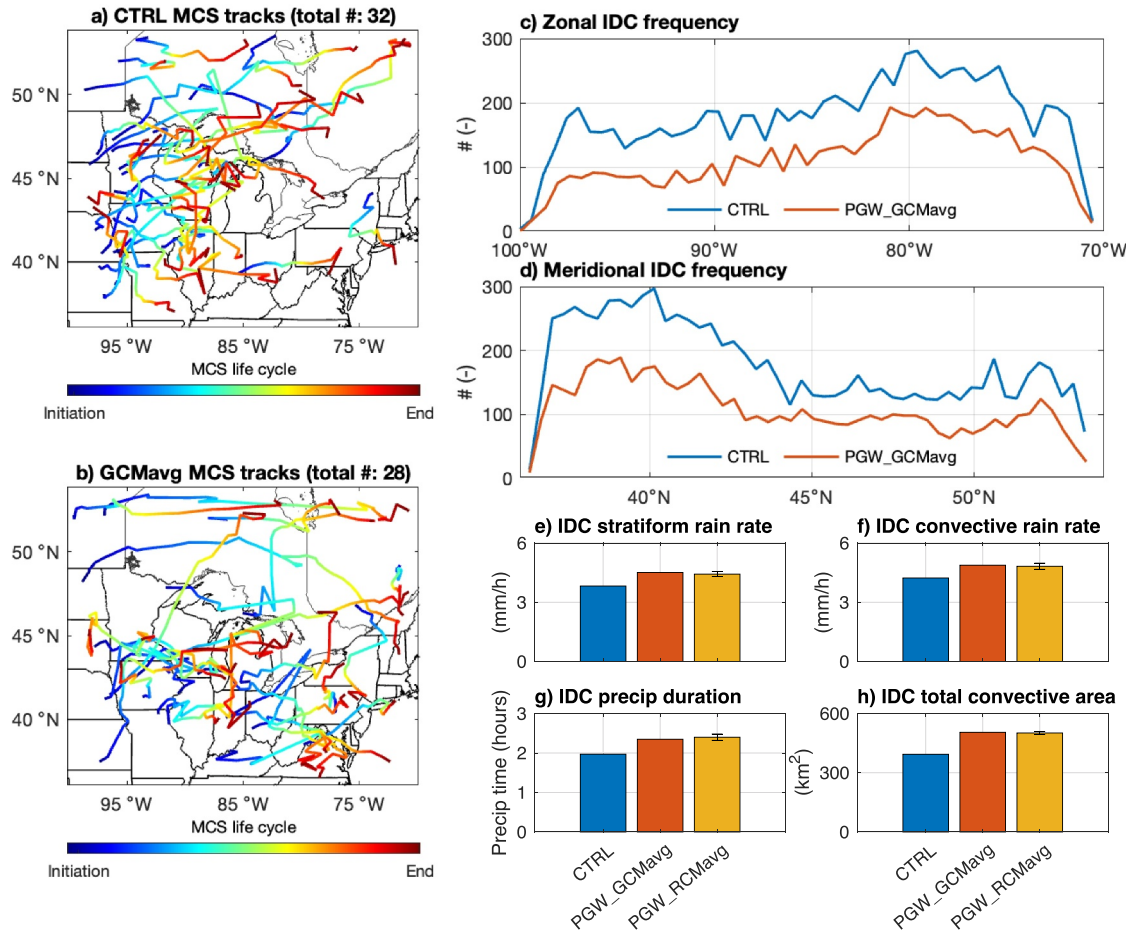


Figure 10. MCS and IDC characteristics for CTRL and PGW_GCMavg. (a) and (b) the MCS tracks from initiation to dissipation through their entire life cycles. (c) and (d) the zonal and meridional frequency of IDCs. (e–h) IDC characteristics including stratiform rain rate, convective rain rate, duration and convective area for CTRL, PGW_GCMavg and PGW_RCMavgs, the error bars in the third columns indicate the standard deviation across different ensemble members.

LCL and LFC changes play more critical roles. Specifically, over places where LCL and LFC are lower, the amount of precipitation is likely to increase for both MCSs and IDCs in the PGW simulations. Our results further suggest that PGW induced moisture and temperature change exert the opposite effect on the LCL and LFC, that is, PGW induced moisture increase is more likely to lower the LCL and LFC whereas PGW induced temperature increase is more likely to lift LCL and LFC.

The cross-section analysis indicates a reduction in ET at the upwind region, likely attributable to the concurrent precipitation decrease. As a result of the decrease in latent heat flux, more energy is partitioned into sensible heat, thus increasing the surface air temperature. The warmer and drier atmosphere at the upwind region become less favorable for convection to occur, as indicated by higher LCL. However, the existence of the Great Lakes serves as an abundant source of moisture for its surrounding and downwind region. The increase in atmospheric moisture lowers the LCL and LFC and thereby facilitating convection, especially for the downwind regions.

While many previous studies utilize the PGW approach with the ensemble mean of GCM deltas providing the future forcing, the uncertainty of ensemble members driven by individual GCMs has rarely been evaluated. In this study, we evaluated the ensemble mean of GCM forcings by running the PGW simulation derived from each individual GCM model and compared with the ensemble mean. Overall, while there exist variabilities in terms of MCS or IDC characteristics among the PGW simulations based on individual GCMs, the mean of simulations driven by each individual GCM forcings is very similar to that of the simulation driven by the mean of GCM forcings. As such, our results indicate that it would be appropriate for future analysis containing more years to

adopt the ensemble mean of GCM forcings to drive RCMs, as our results show that this approach would adequately capture the overarching signals and physical mechanism induced by perturbations.

While this study analyzes one summer in 2018, the findings are important due to the following reasons. First, 2018 was a neutral year over the GLR, and its MCS and IDC patterns are similar to the multi-year climatology, as presented in Wang et al. (2022). Second, the 12 ensemble members in the PGW simulations show consistent results in terms of the future summer precipitation changes although the magnitude varies across ESMs. While we present the ensemble mean results in the main manuscript, all analyses have been done for each ensemble member, and results are consistent between all ensemble members. This suggests that the physical mechanisms, for both the MCS and IDC precipitation changes, are consistent across all the ensemble members.

Data Availability Statement

To evaluate the simulated precipitation, the PRISM precipitation data (Daly et al., 2008; accessed Mar. 2023), the TRMM data (Huffman et al., 2007; accessed Jun. 2023), and the Stage IV precipitation (Fulton et al., 1998; Seo & Breidenbach, 2002; accessed Jun. 2023) are used. Description of the convective precipitation data set is available from (Li et al., 2021; accessed Aug. 2023). Our code repository can be found at Yang (2024).

References

- Adachi, S. A., & Tomita, H. (2020). Methodology of the constraint condition in dynamical downscaling for regional climate evaluation: A review. *Journal of Geophysical Research: Atmospheres*, 125(11), e2019JD032166. <https://doi.org/10.1029/2019jd032166>
- Arsenault, K. R., Nearing, G. S., Wang, S., Yatheendradas, S., & Peters-Lidard, C. D. (2018). Parameter sensitivity of the noah-MP land surface model with dynamic vegetation. *Journal of Hydrometeorology*, 19(5), 815–830. <https://doi.org/10.1175/JHM-D-17-0205.1>
- Barlage, M., Chen, F., Rasmussen, R., Zhang, Z., & Miguez-Macho, G. (2021). The importance of scale-dependent groundwater processes in land-atmosphere interactions over the Central United States. *Geophysical Research Letters*, 48(5), e2020GL092171. <https://doi.org/10.1029/2020GL092171>
- Basile, S. J., Rauscher, S. A., & Steiner, A. L. (2017). Projected precipitation changes within the Great lakes and western lake erie basin: A multi-model analysis of intensity and seasonality. *International Journal of Climatology*, 37(14), 4864–4879. <https://doi.org/10.1002/joc.5128>
- Bates, G. T., Giorgi, F., & Hostetler, S. W. (1993). Toward the simulation of the effects of the Great lakes on regional climate. *Monthly Weather Review*, 121(5), 1373–1387. [https://doi.org/10.1175/1520-0493\(1993\)121<1373:tsote>2.0.co;2](https://doi.org/10.1175/1520-0493(1993)121<1373:tsote>2.0.co;2)
- Bi, D., Dix, M., Marsland, S., O'Farrell, S., Sullivan, A., Bodman, R., et al. (2020). Configuration and spin-up of ACCESS-CM2, the new generation Australian community climate and earth system simulator coupled model. *Journal of Southern Hemisphere Earth Systems Science*, 70(1), 225–251. <https://doi.org/10.1071/ES19040>
- Boucher, O., Servonnat, J., Albright, A. L., Aumont, O., Balkanski, Y., Bastrikov, V., et al. (2020). Presentation and evaluation of the IPSL-CM6A-LR climate model. *Journal of Advances in Modeling Earth Systems*, 12(7), e2019MS002010. <https://doi.org/10.1029/2019MS002010>
- Briley, L. J., Rood, R. B., & Notaro, M. (2021). Large lakes in climate models: A Great lakes case study on the usability of CMIP5. *Journal of Great Lakes Research*, 47(2), 405–418. <https://doi.org/10.1016/j.jglr.2021.01.010>
- Brogli, R., Heim, C., Mensch, J., Sørland, S. L., & Schär, C. (2023). The pseudo-global-warming (PGW) approach: Methodology, software package PGW4ERA5 v1.1, validation, and sensitivity analyses. *Geoscientific Model Development*, 16(3), 907–926. <https://doi.org/10.5194/gmd-16-907-2023>
- Bryan, A. M., Steiner, A. L., & Posselt, D. J. (2015). Regional modeling of surface-atmosphere interactions and their impact on Great Lakes hydroclimate. *Journal of Geophysical Research*, 120(3), 1044–1064. <https://doi.org/10.1002/2014JD022316>
- Byun, K., Sharma, A., Wang, J., Tank, J. L., & Hamlet, A. F. (2022). Intercomparison of dynamically and statistically downscaled climate change projections over the midwest and Great lakes region. *Journal of Hydrometeorology*, 23(5), 659–679. <https://doi.org/10.1175/jhm-d-20-0282.1>
- Chen, F., & Dudhia, J. (2001). Coupling an advanced land surface-hydrology model with the Penn State-NCAR MM5 modeling system. Part I: Model implementation and sensitivity. *Monthly Weather Review*, 129(4), 569–585. [https://doi.org/10.1175/1520-0493\(2001\)129<0587:caalsh>2.0.co;2](https://doi.org/10.1175/1520-0493(2001)129<0587:caalsh>2.0.co;2)
- Chen, J., Dai, A., & Zhang, Y. (2020). Linkage between projected precipitation and atmospheric thermodynamic changes. *Journal of Climate*, 33(16), 7155–7178. <https://doi.org/10.1175/jcli-d-19-0785.1>
- Chen, J., Dai, A., Zhang, Y., & Rasmussen, K. L. (2019). Changes in convective available potential energy and convective inhibition under global warming changes in convective available potential energy and convective inhibition under global warming. *Journal of Climate*, 33(6), 2025–2050. <https://doi.org/10.1175/jcli-d-19-0461.1>
- Cherchi, A., Fogli, P. G., Lovato, T., Peano, D., Iovino, D., Gualdi, S., et al. (2019). Global mean climate and main patterns of variability in the CMCC-CM2 coupled model. *Journal of Advances in Modeling Earth Systems*, 11(1), 185–209. <https://doi.org/10.1029/2018MS001369>
- Cherkauer, K. A., & Sinha, T. (2010). Hydrologic impacts of projected future climate change in the Lake Michigan region. *Journal of Great Lakes Research*, 36(SP2), 33–50. <https://doi.org/10.1016/j.jglr.2009.11.012>
- Daly, C., Halbleib, M., Smith, J. I., Gibson, W. P., Doggett, M. K., Taylor, G. H., et al. (2008). Physiographically sensitive mapping of climatological temperature and precipitation across the conterminous United States [Dataset]. *International Journal of Climatology*, 28(15), 2031–2064. <https://doi.org/10.1002/joc.1688>
- Danabasoglu, G., Lamarque, J. F., Bacmeister, J., Bailey, D., DuVivier, A., Edwards, J., et al. (2020). The community earth system model version 2 (CESM2). *Journal of Advances in Modeling Earth Systems*, 12(2), e2019MS001916. <https://doi.org/10.1029/2019MS001916>
- Del Genio, A. D., & Kovari, W. (2002). Climatic properties of tropical precipitating convection under varying environmental conditions. *Journal of Climate*, 15(18), 2597–2615. [https://doi.org/10.1175/1520-0442\(2002\)015<2597:CPOTPC>2.0.CO;2](https://doi.org/10.1175/1520-0442(2002)015<2597:CPOTPC>2.0.CO;2)
- Diffenbaugh, N. S., Scherer, M., & Trapp, R. J. (2013). Robust increases in severe thunderstorm environments in response to greenhouse forcing. *Proceedings of the National Academy of Sciences*, 110(41), 16361–16366. <https://doi.org/10.1073/pnas.1307758110>

Acknowledgments

This research is based on work supported by COMPASS-GLM, a multi-institutional project supported by the U.S. Department of Energy, Office of Science, Office of Biological and Environmental Research as part of the Regional and Global Modeling and Analysis (RGMA) program, Multi-sector Dynamics Modeling (MSD) program, and Earth System Model Development (ESMD) program. This is Contribution No. 123 of the Great Lakes Research Center at Michigan Tech. Computational resources are provided by the DOE-supported National Energy Research Scientific Computing Center. The Pacific Northwest National Laboratory is operated for DOE by Battelle Memorial Institute under contract DE-AC05-76RL01830. Argonne National Laboratory is a US Department of Energy laboratory managed by UChicago Argonne, LLC, under contract DE-AC02-06CH11357.

- d'Orgeville, M., Peltier, W. R., Erler, A. R., & Gula, J. (2014). Climate change impacts on Great Lakes Basin precipitation extremes. *Journal of Geophysical Research: Atmospheres*, *119*(18), 10799–10812. <https://doi.org/10.1002/2014JD021855>
- Dougherty, E. M., Prein, A. F., Gutmann, E. D., & Newman, A. J. (2023). Future simulated changes in central U.S. Mesoscale convective system rainfall caused by changes in convective and stratiform structure. *Journal of Geophysical Research: Atmospheres*, *128*(4), e2022JD037537. <https://doi.org/10.1029/2022JD037537>
- Feng, Z., Jr, R. A. H., Leung, L. R., Song, F., Hardin, J. C., Wang, J., et al. (2019). Spatiotemporal characteristics and large-scale environments of mesoscale convective systems east of the rocky mountains. *Journal of Climate*, *32*(21), 7303–7328. <https://doi.org/10.1175/jcli-d-19-0137.1>
- Feng, Z., Leung, L. R., Jr, R. A. H., Hagos, S., Hardin, J., Yang, Q., et al. (2018). Structure and evolution of mesoscale convective systems: Sensitivity to cloud microphysics in convection-permitting simulations over the United States. *Journal of Advances in Modeling Earth Systems*, *10*(7), 1470–1494. <https://doi.org/10.1029/2018ms001305>
- Fulton, R. A., Breidenbach, J. P., Seo, D.-J., Miller, D. A., & O'Bannon, T. (1998). The WSR-88D rainfall algorithm [Dataset]. *Weather and Forecasting*, *13*(2), 377–395. [https://doi.org/10.1175/1520-0434\(1998\)013<0377:twra>2.0.co;2](https://doi.org/10.1175/1520-0434(1998)013<0377:twra>2.0.co;2)
- Gensini, V. A., & Mote, T. L. (2015). Downscaled estimates of late 21st century severe weather from CCSM3. *Climatic Change*, *129*(1–2), 307–321. <https://doi.org/10.1007/s10584-014-1320-z>
- Golaz, J. C., Caldwell, P. M., Van Roekel, L. P., Petersen, M. R., Tang, Q., Wolfe, J. D., et al. (2019). The DOE E3SM coupled model version 1: Overview and evaluation at standard resolution. *Journal of Advances in Modeling Earth Systems*, *11*(7), 2089–2129. <https://doi.org/10.1029/2018MS001603>
- Gronewold, A. D., Fortin, V., Lofgren, B., Clites, A., Stow, C. A., & Quinn, F. (2013). Coasts, water levels, and climate change: A Great lakes perspective. *Climatic Change*, *120*(4), 697–711. <https://doi.org/10.1007/s10584-013-0840-2>
- Gronewold, A. D., & Stow, C. A. (2014). Water loss from the Great lakes. *Science*, *343*(6175), 1084–1085. <https://doi.org/10.1126/science.1249978>
- Gutmann, E. D., Rasmussen, R. M., Liu, C., Ikeda, K., Bruyere, C. L., Done, J. M., et al. (2018). Changes in hurricanes from a 13-Yr convection-permitting pseudo-global warming simulation. *Journal of Climate*, *31*(9), 3643–3657. <https://doi.org/10.1175/jcli-d-17-0391.1>
- Hara, M., Yoshikane, T., Kawase, H., & Kimura, F. (2008). Estimation of the impact of global warming on snow Depth in Japan by the pseudo-global-warming method. *Hydrological Research Letters*, *2*, 61–64. <https://doi.org/10.3178/hrl.2.61>
- He, B., Bao, Q., Wang, X., Zhou, L., Wu, X., Liu, Y., et al. (2019). CAS FGOALS-f3-L model datasets for CMIP6 historical atmospheric model intercomparison project simulation. *Advances in Atmospheric Sciences*, *36*(8), 771–778. <https://doi.org/10.1007/s00376-019-9027-8>
- Held, I., Guo, H., Adcroft, A., Dunne, J., Horowitz, L., Krasting, J., et al. (2019). Structure and performance of GFDL's CM4. 0 climate model. *Journal of Advances in Modeling Earth Systems*, *11*(11), 3691–3727. <https://doi.org/10.1029/2019MS001829>
- Hersbach, H., Bell, B., Berrisford, P., Hirahara, S., Horányi, A., Muñoz-Sabater, J., et al. (2020). The ERA5 global reanalysis. *Quarterly Journal of the Royal Meteorological Society*, *146*(730), 1999–2049. <https://doi.org/10.1002/qj.3803>
- Hoogewind, K. A., Baldwin, M. E., & Trapp, R. J. (2017). The impact of climate change on Hazardous convective weather in the United States: Insight from high-resolution dynamical downscaling. *Journal of Climate*, *30*(24), 10081–10100. <https://doi.org/10.1175/jcli-d-16-0885.1>
- Hu, H., Leung, L. R., & Feng, Z. (2020). Understanding the distinct impacts of MCS and non-MCS rainfall on the surface water balance in the Central United States using a numerical water-tagging technique. *Journal of Hydrometeorology*, *21*(10), 2343–2357. <https://doi.org/10.1175/JHM-D-20-0081.1>
- Huffman, G. J., Bolvin, D. T., Nelkin, E. J., Wolff, D. B., Adler, R. F., Gu, G., et al. (2007). The TRMM multisatellite precipitation analysis (TMPA): Quasi-global, Multiyear, Combined-Sensor precipitation estimates at fine scales [Dataset]. *Journal of Hydrometeorology*, *8*(1), 38–55. <https://doi.org/10.1175/jhm560.1>
- Iacono, M. J., Delamere, J. S., Mlawer, E. J., Shephard, M. W., Clough, S. A., & Collins, W. D. (2008). Radiative forcing by long-lived greenhouse gases: Calculations with the AER radiative transfer models. *Journal of Geophysical Research: Atmosphere*, *113*(D13), D13103. <https://doi.org/10.1029/2008jd009944>
- Ito, R., Takemi, T., & Arakawa, O. (2016). A possible reduction in the Severity of Typhoon wind in the northern part of Japan under global warming: A case study. *SOLA*, *12*(0), 100–105. <https://doi.org/10.2151/sola.2016-023>
- Janjić, Z. I. (1990). The step-mountain coordinate: Physical package. *Monthly Weather Review*, *118*(7), 1429–1443. [https://doi.org/10.1175/1520-0493\(1990\)118<1429:TSMCPP>2.0.CO;2](https://doi.org/10.1175/1520-0493(1990)118<1429:TSMCPP>2.0.CO;2)
- Janjić, Z. I. (1994). The step-Mountain Eta coordinate model: Further developments of the convection, viscous sublayer, and turbulence closure schemes. *Monthly Weather Review*, *122*(5), 927–945. [https://doi.org/10.1175/1520-0493\(1994\)122<0927:tsmecm>2.0.co;2](https://doi.org/10.1175/1520-0493(1994)122<0927:tsmecm>2.0.co;2)
- Kayastha, M. B., Ye, X., Huang, C., & Xue, P. (2022). Future rise of the Great Lakes water levels under climate change. *Journal of Hydrology*, *612*, 128205. <https://doi.org/10.1016/j.jhydrol.2022.128205>
- Kendon, E. J., Roberts, N. M., Senior, C. A., & Roberts, M. J. (2012). Realism of rainfall in a very high-resolution regional climate model. *Journal of Climate*, *25*(17), 5791–5806. <https://doi.org/10.1175/JCLI-D-11-00562.1>
- Lenderink, G., Barbero, R., Loriaux, J. M., & Fowler, H. J. (2017). Super-clausius–clapeyron scaling of extreme hourly convective precipitation and its relation to large-scale atmospheric conditions. *Journal of Climate*, *30*(15), 6037–6052. <https://doi.org/10.1175/JCLI-D-16-0808.1>
- Lenderink, G., & van Meijgaard, E. (2008). Increase in hourly precipitation extremes beyond expectations from temperature changes. *Nature Geoscience*, *1*(8), 511–514. <https://doi.org/10.1038/ngeo262>
- Lenderink, G., & van Meijgaard, E. (2010). Linking increases in hourly precipitation extremes to atmospheric temperature and moisture changes. *Environmental Research Letters*, *5*(2), 025208. <https://doi.org/10.1088/1748-9326/5/2/025208>
- Li, J., Feng, Z., Qian, Y., & Leung, L. R. (2021). A high-resolution unified observational data product of mesoscale convective systems and isolated deep convection in the United States for 2004–2017 [Dataset]. *Earth System Science Data*, *13*(2), 827–856. <https://doi.org/10.5194/essd-13-827-2021>
- Li, X., Zhong, S., Bian, X., Heilman, W. E., Luo, Y., & Dong, W. (2010). Hydroclimate and variability in the Great lakes region as derived from the north American regional reanalysis. *Journal of Geophysical Research*, *115*(D12), D12104. <https://doi.org/10.1029/2009JD012756>
- Liu, C., Ikeda, K., Rasmussen, R., Barlage, M., Newman, A. J., Prein, A. F., et al. (2017). Continental-scale convection-permitting modeling of the current and future climate of North America. *Climate Dynamics*, *49*(1–2), 71–95. <https://doi.org/10.1007/s00382-016-3327-9>
- Lynn, B., Healy, R., & Druyan, L. (2009). Investigation of Hurricane Katrina characteristics for future, warmer climates. *Climate Research*, *39*(June), 75–86. <https://doi.org/10.3354/cr00801>
- Mahoney, K., Alexander, M., Scott, J. D., & Barsugli, J. (2013). High-resolution downscaled simulations of warm-season extreme precipitation events in the Colorado front range under past and future climates. *Journal of Climate*, *26*(21), 8671–8689. <https://doi.org/10.1175/JCLI-D-12-00744.1>

- Mauritsen, T., Bader, J., Becker, T., Behrens, J., Bittner, M., Brokopf, R., et al. (2019). Developments in the MPI-M earth system model version 1.2 (MPI-ESM1.2) and its response to increasing CO₂. *Journal of Advances in Modeling Earth Systems*, 11(4), 998–1038. <https://doi.org/10.1029/2018MS001400>
- Michalak, A. M., Anderson, E. J., Beletsky, D., Boland, S., Bosch, N. S., Bridgeman, T. B., et al. (2013). Record-setting algal bloom in Lake Erie caused by agricultural and meteorological trends consistent with expected future conditions. *Proceedings of the National Academy of Sciences*, 110(16), 6448–6452. <https://doi.org/10.1073/pnas.1216006110>
- Minallah, S., & Steiner, A. L. (2021). Analysis of the atmospheric water cycle for the Laurentian Great lakes region using CMIP6 models. *Journal of Climate*, 34(12), 4693–4710. <https://doi.org/10.1175/JCLI-D-20-0751.1>
- Mishra, V., & Cherkauer, K. A. (2011). Influence of cold season climate variability on lakes and wetlands in the Great Lakes region. *Journal of Geophysical Research*, 116(D12), D12111. <https://doi.org/10.1029/2010JD015063>
- Nelson, B. R., Prat, O. P., Seo, D. J., & Habib, E. (2016). Assessment and implications of NCEP stage IV Quantitative precipitation estimates for product intercomparisons. *Weather and Forecasting*, 31(2), 371–394. <https://doi.org/10.1175/waf-d-14-00112.1>
- Niu, G.-Y., Yang, Z.-L., Mitchell, K. E., Chen, F., Ek, M. B., Barlage, M., et al. (2011). The community Noah land surface model with multiparameterization options (Noah-MP): 1. Model description and evaluation with local-scale measurements. *Journal of Geophysical Research*, 116(D12), D12109. <https://doi.org/10.1029/2010jd015139>
- Notaro, M., Holman, K., Zarrin, A., Fluck, E., Vavrus, S., & Bennington, V. (2013). Influence of the Laurentian Great lakes on regional climate. *Journal of Climate*, 26(3), 789–804. <https://doi.org/10.1175/JCLI-D-12-00140.1>
- Notaro, M., Jorns, J., & Briley, L. (2022). Representation of lake–atmosphere interactions and Lake-effect snowfall in the Laurentian Great Lakes Basin among HighResMIP global climate models. *Journal of the Atmospheric Sciences*, 79(5), 1325–1347. <https://doi.org/10.1175/JAS-D-21-0249.1>
- Notaro, M., Zhong, Y., Xue, P., Peters-Lidard, C., Cruz, C., Kemp, E., et al. (2021). Cold season performance of the NU-WRF regional climate model in the Great Lakes Region. *Journal of Hydrometeorology*, 22(9), 2423–2454. <https://doi.org/10.1175/JHM-D-21-0025.1>
- O’Gorman, P. A., & Schneider, T. (2009). Scaling of precipitation extremes over a wide range of climates simulated with an idealized GCM. *Journal of Climate*, 22(21), 5676–5685. <https://doi.org/10.1175/2009JCLI2701.1>
- Pall, P., Allen, M. R., & Stone, D. A. (2007). Testing the Clausius–Clapeyron constraint on changes in extreme precipitation under CO₂ warming. *Climate Dynamics*, 28(4), 351–363. <https://doi.org/10.1007/s00382-006-0180-2>
- Pendergrass, A. G. (2018). What precipitation is extreme? *Science*, 360(6393), 1072–1073. <https://doi.org/10.1126/science.aat1871>
- Pendergrass, A. G. (2020). The global-mean precipitation response to CO₂-induced warming in CMIP6 models. *Geophysical Research Letters*, 47(17). <https://doi.org/10.1029/2020GL089964>
- Pendergrass, A. G., & Hartmann, D. L. (2014). Changes in the distribution of rain frequency and intensity in response to global warming. *Journal of Climate*, 27(22), 8372–8383. <https://doi.org/10.1175/JCLI-D-14-00183.1>
- Pendergrass, A. G., Knutti, R., Lehner, F., Deser, C., & Sanderson, B. M. (2017). Precipitation variability increases in a warmer climate. *Scientific Reports*, 7(1), 17966. <https://doi.org/10.1038/s41598-017-17966-y>
- Peters, J. M., Nielsen, E. R., Parker, M. D., Hitchcock, S. M., & Schumacher, R. S. (2017). The impact of low-level moisture errors on model forecasts of an MCS observed during PECAN. *Monthly Weather Review*, 145(9), 3599–3624. <https://doi.org/10.1175/mwr-d-16-0296.1>
- Prein, A. F., Liu, C., Ikeda, K., Bullock, R., Rasmussen, R. M., Holland, G. J., & Clark, M. (2020). Simulating North American mesoscale convective systems with a convection-permitting climate model. *Climate Dynamics*, 55(1–2), 95–110. <https://doi.org/10.1007/s00382-017-3993-2>
- Prein, A. F., Rasmussen, R. M., Ikeda, K., Liu, C., Clark, M. P., & Holland, G. J. (2017). The future intensification of hourly precipitation extremes. *Nature Climate Change*, 7(1), 48–52. <https://doi.org/10.1038/nclimate3168>
- Rasmussen, K. L., Prein, A. F., Rasmussen, R. M., Ikeda, K., & Liu, C. (2020). Changes in the convective population and thermodynamic environments in convection-permitting regional climate simulations over the United States. *Climate Dynamics*, 55(1–2), 383–408. <https://doi.org/10.1007/s00382-017-4000-7>
- Rasmussen, R., Liu, C., Ikeda, K., Gochis, D., Yates, D., Chen, F., et al. (2011). High-resolution coupled climate runoff simulations of seasonal snowfall over Colorado: A process study of current and warmer climate. *Journal of Climate*, 24(12), 3015–3048. <https://doi.org/10.1175/2010jcli3985.1>
- Riahi, K., Van Vuuren, D. P., Kriegler, E., Edmonds, J., O’Neill, B. C., Fujimori, S., et al. (2017). The Shared Socioeconomic Pathways and their energy, land use, and greenhouse gas emissions implications: An overview. *Global Environmental Change*, 42, 153–168. <https://doi.org/10.1016/j.gloenvcha.2016.05.009>
- Salamanca, F., Krpo, A., Martilli, A., & Clappier, A. (2010). A new building energy model coupled with an urban canopy parameterization for urban climate simulations—Part I. Formulation, verification, and sensitivity analysis of the model. *Theoretical and Applied Climatology*, 99(3–4), 331–344. <https://doi.org/10.1007/s00704-009-0142-9>
- Salamanca, F., & Martilli, A. (2010). A new building energy model coupled with an urban canopy parameterization for urban climate simulations—Part II. Validation with one dimension off-line simulations. *Theoretical and Applied Climatology*, 99(3–4), 345–356. <https://doi.org/10.1007/s00704-009-0143-8>
- Sato, T., Kimura, F., & Kitoh, A. (2007). Projection of global warming onto regional precipitation over Mongolia using a regional climate model. *Journal of Hydrology*, 333(1), 144–154. <https://doi.org/10.1016/j.jhydrol.2006.07.023>
- Schär, C., Frei, C., Lüthi, D., & Davies, H. C. (1996). Surrogate climate-change scenarios for regional climate models. *Geophysical Research Letters*, 23(6), 669–672. <https://doi.org/10.1029/96gl00265>
- Schumacher, R. S., & Peters, J. M. (2017). Near-surface thermodynamic sensitivities in simulated extreme-rain-producing mesoscale convective systems. *Monthly Weather Review*, 145(6), 2177–2200. <https://doi.org/10.1175/mwr-d-16-0255.1>
- Schwab, D. J., Leshkevich, G. A., & Muhr, G. C. (1992). Satellite measurements of surface water temperature in the Great lakes: Great lakes coastwatch. *Journal of Great Lakes Research*, 18(2), 247–258. [https://doi.org/10.1016/s0380-1330\(92\)71292-1](https://doi.org/10.1016/s0380-1330(92)71292-1)
- Scott, R. W., & Huff, F. A. (1996). Impacts of the Great lakes on regional climate conditions. *Journal of Great Lakes Research*, 22(4), 845–863. [https://doi.org/10.1016/S0380-1330\(96\)71006-7](https://doi.org/10.1016/S0380-1330(96)71006-7)
- Seeley, J. T., & Romps, D. M. (2015). Why does tropical convective available potential energy (CAPE) increase with warming? *Geophysical Research Letters*, 42(23), 10429–10437. <https://doi.org/10.1002/2015GL066199>
- Seland, Ø., Bentsen, M., Olivie, D. J. L., Toniazzo, T., Gjermundsen, A., Graff, L. S., et al. (2020). Overview of the Norwegian Earth System Model (NorESM2) and key climate response of CMIP6 DECK, historical, and scenario simulations. *Geoscientific Model Development*, 13(12), 6165–6200. <https://doi.org/10.5194/gmd-13-6165-2020>
- Seo, D. J., & Breidenbach, J. P. (2002). Real-time correction of spatially nonuniform bias in radar rainfall data using rain gauge measurements [Dataset]. *Journal of Hydrometeorology*, 3(2), 93–111. [https://doi.org/10.1175/1525-7541\(2002\)003<0093:rtcoss>2.0.co;2](https://doi.org/10.1175/1525-7541(2002)003<0093:rtcoss>2.0.co;2)

- Sharma, A., Hamlet, A. F., Fernando, H. J. S., Catlett, C. E., Horton, D. E., Kotamarthi, V. R., et al. (2018). The need for an integrated land-lake-atmosphere modeling system, exemplified by north America's Great lakes region. *Earth's Future*, 6(10), 1366–1379. <https://doi.org/10.1029/2018EF000870>
- Sheffield, J., & Wood, E. F. (2008). Projected changes in drought occurrence under future global warming from multi-model, multi-scenario, IPCC AR4 simulations. *Climate Dynamics*, 31(1), 79–105. <https://doi.org/10.1007/s00382-007-0340-z>
- Shepherd, T. G. (2019). Storyline approach to the construction of regional climate change information. *Proceedings of the Royal Society A*, 475(2225), 20190013. <https://doi.org/10.1098/rspa.2019.0013>
- Shi, Q., & Xue, P. (2019). Impact of lake surface temperature variations on lake effect snow over the Great Lakes region. *Journal of Geophysical Research: Atmospheres*, 124(23), 12553–12567. <https://doi.org/10.1029/2019JD031261>
- Skamarock, W. C., Klemp, J. B., Dudhia, J., Gill, D. O., Barker, D. M., Duda, M. G., et al. (2008). A description of the advanced research WRF version 3. *NCAR Technical Note*. <https://doi.org/10.5065/d68s4mvh>
- Starzec, M., Homeyer, C. R., & Mullendore, G. L. (2017). Storm labeling in three dimensions (SL3D): A volumetric radar echo and dual-polarization updraft classification algorithm. *Monthly Weather Review*, 145(3), 1127–1145. <https://doi.org/10.1175/MWR-D-16-0089.1>
- Swart, N. C., Cole, J. N. S., Kharin, V. V., Lazare, M., Scinocca, J. F., Gillett, N. P., et al. (2019). The Canadian earth system model version 5 (CanESM5. 0.3). *Geoscientific Model Development*, 12(11), 4823–4873. <https://doi.org/10.5194/gmd-12-4823-2019>
- Tatebe, H., Ogura, T., Nitta, T., Komuro, Y., Ogochi, K., Takemura, T., et al. (2019). Description and basic evaluation of simulated mean state, internal variability, and climate sensitivity in MIROC6. *Geoscientific Model Development*, 12(7), 2727–2765. <https://doi.org/10.5194/gmd-12-2727-2019>
- Thompson, G., Field, P. R., Rasmussen, R. M., & Hall, W. D. (2008). Explicit forecasts of winter precipitation using an improved bulk microphysics scheme. Part II: Implementation of a new snow parameterization. *Monthly Weather Review*, 136(12), 5095–5115. <https://doi.org/10.1175/2008mwr2387.1>
- Thompson, G., Rasmussen, R. M., & Manning, K. (2004). Explicit forecasts of winter precipitation using an improved bulk microphysics scheme. Part I: Description and sensitivity analysis. *Monthly Weather Review*, 132(2), 519–542. [https://doi.org/10.1175/1520-0493\(2004\)132<0519:EFOWPU>2.0.CO;2](https://doi.org/10.1175/1520-0493(2004)132<0519:EFOWPU>2.0.CO;2)
- Tidwell, V. C., & Pebbles, V. (2015). The water-energy-environment nexus in the Great lakes region: The case for integrated resource planning. *Energy and Environment Research*, 5(2), 1. <https://doi.org/10.5539/eer.v5n2p1>
- Trapp, R. J., Woods, M. J., Lasher-Trapp, S. G., & Grover, M. A. (2021). Alternative implementations of the “Pseudo-global-warming” methodology for event-based simulations. *Journal of Geophysical Research: Atmospheres*, 126(24), e2021JD035017. <https://doi.org/10.1029/2021jd035017>
- Trenberth, K. (2011). Changes in precipitation with climate change. *Climate Research*, 47(1), 123–138. <https://doi.org/10.3354/cr00953>
- Trenberth, K. E., Dai, A., Rasmussen, R. M., & Parsons, D. B. (2003). The changing character of precipitation. *Bulletin American Meteorology Society*, 84(9), 1205–1218. <https://doi.org/10.1175/BAMS-84-9-1205>
- Wang, J., Qian, Y., Pringle, W., Chakraborty, T. C., Hetland, R., Yang, Z., & Xue, P. (2023). Contrasting effects of lake breeze and urbanization on heat stress in Chicago metropolitan area. *Urban Climate*, 48, 101429. <https://doi.org/10.1016/j.uclim.2023.101429>
- Wang, J., Xue, P., Pringle, W., Yang, Z., & Qian, Y. (2022). Impacts of lake surface temperature on the summer climate over the Great lakes region. *Journal of Geophysical Research: Atmospheres*, 127(11), e2021JD036231. <https://doi.org/10.1029/2021JD036231>
- Westra, S., Fowler, H. J., Evans, J. P., Alexander, L. V., Berg, P., Johnson, F., et al. (2014). Future changes to the intensity and frequency of short-duration extreme rainfall. *Reviews of Geophysics*, 52(3), 522–555. <https://doi.org/10.1002/2014RG000464>
- Workoff, T. E., Kristovich, D. A. R., Laird, N. F., Laplante, R., & Leins, D. (2012). Influence of the lake Erie overlake boundary layer on deep convective storm evolution. *Weather and Forecasting*, 27(5), 1279–1289. <https://doi.org/10.1175/waf-d-11-00076.1>
- Xue, P., Malanotte-Rizzoli, P., Wei, J., & Eltahir, E. A. B. (2020). Coupled ocean-Atmosphere modeling over the maritime continent: A review. *Journal of Geophysical Research: Oceans*, 125(6), e2019JC014978. <https://doi.org/10.1029/2019JC014978>
- Xue, P., Pal, J. S., Ye, X., Lenters, J. D., Huang, C., & Chu, P. Y. (2017). Improving the simulation of large lakes in regional climate modeling: Two-way lake-atmosphere coupling with a 3D hydrodynamic model of the Great lakes. *Journal of Climate*, 30(5), 1605–1627. <https://doi.org/10.1175/JCLI-D-16-0225.1>
- Xue, P., Ye, X., Pal, J. S., Chu, P. Y., Kayastha, M. B., & Huang, C. (2022). Climate projections over the Great lakes region: Using two-way coupling of a regional climate model with a 3-D lake model. *Geoscientific Model Development Discussions*, 2022, 1–37. <https://doi.org/10.5194/gmd-2021-440>
- Yang, Z. (2024). Summer precipitation changes over the Great lakes region under a warming scenario (version V1) [Dataset]. *Zenodo*. <https://doi.org/10.5281/zenodo.10594123>
- Yang, Z., Qian, Y., Xue, P., Wang, J., Chakraborty, T. C., Pringle, W. J., et al. (2023). Moisture sources of precipitation in the Great lakes region: Climatology and recent changes. *Geophysical Research Letters*, 50(5), e2022GL100682. <https://doi.org/10.1029/2022gl100682>
- Yang, Z., Varble, A., Berg, L. K., Qian, Y., Tai, S.-L., Chen, J., et al. (2023). Sensitivity of precipitation displacement of a simulated MCS to changes in land surface conditions. *Journal of Geophysical Research: Atmospheres*, 128(10), e2022JD037642. <https://doi.org/10.1029/2022JD037642>
- Zobel, Z., Wang, J., Wuebbles, D. J., & Kotamarthi, V. R. (2018). Analyses for high-resolution projections through the end of the 21st century for precipitation extremes over the United States. *Earth's Future*, 6(10), 1471–1490. <https://doi.org/10.1029/2018EF000956>